A 3-D shear velocity model of the crust and uppermost mantle beneath Alaska including apparent radial anisotropy

Lili Feng and Michael H. Ritzwoller

Department of Physics, University of Colorado at Boulder, Boulder, CO 80309 USA

Corresponding author: Lili Feng (lili.feng@colorado.edu)

Key Points:

- A 3-D radially anisotropic model beneath Alaska is constructed by Bayesian Monte Carlo inversion.
- The Vsv part of the model captures many geological and tectonic features, including the Alaskan subduction zone and the cratonic roots.
- The crustal radial anisotropy is strongest across areas that were subjected to significant extensional deformation in the Cretaceous.

Abstract

This paper presents a model of the 3-D shear velocity structure of the crust and uppermost mantle beneath Alaska and surroundings on a ~50 km grid, including crustal and mantle radial anisotropy, based on seismic data recorded at more than 500 broadband stations. The model derives from a Bayesian Monte Carlo inversion of Rayleigh wave group and phase speeds and Love wave phase speeds determined from ambient noise and earthquake data. Prominent features resolved in the model include: (1) Apparent crustal radial anisotropy is strongest across the parts of central and northern Alaska that were subject to significant extension during the Cretaceous, consistent with crustal anisotropy being caused by deformationally-aligned middle to lower crustal sheet silicates (micas) with shallowly dipping foliation planes beneath extensional domains. (2) Crustal thickness estimates are similar to those from receiver functions by Miller & Moresi (2018). (3) Very thick lithosphere underlies Arctic-Alaska, with high shear wave speeds that extend at least to 120 km depth, which may challenge rotational transport models for the evolution of the region. (4) Subducting lithosphere beneath Alaska is resolved, including what we call the "Barren Islands slab anomaly", an "aseismic slab edge" north of the Denali Volcanic Gap, the "Wrangellia slab anomaly", and Yakutat lithosphere subducting seaward of the Wrangell volcanic field. (5) The geometry of the Alaskan subduction zone generally agrees with the slab model Alaska_3D 1.0 of Jadamec & Billen (2010) except for the Yakutat "slab shoulder region", which is newly imaged in our model.

1. Introduction

Alaska is a region composed of crustal fragments squeezed between the Siberian and Laurentian cratons. It is characterized by a particularly variable crust that was built by subduction, large block rotation in the north (e.g., Moore and Box, 2016), extensional tectonics (e.g., Johnston, 2001), and the successive accretion of terranes along both convergent and strike-slip fault systems in the south (e.g., Coney & Jones, 1985; Johnston, 2001). The active southern margin of Alaska is particularly complex, and tectonic growth is on-going due to the underthrusting of the Pacific plate in the Alaska-Aleutian subduction zone and the collisional orogeny produced by the Yakutat crustal block as shown in **Figure 1a**, which is intersecting and subducting beneath at least parts of central Alaska (e.g., Jadamec and Billen, 2010; Haynie and Jadamec, 2017). The Yakutat microplate (**Fig. 1b,** modified from Eberhart-Philips et al., 2006), is the most recent exotic terrane assimilated onto the North American continent. All parts of Alaska continue to move relative to stable North America and active seismicity is found across most of the state (Freymueller et al., 2008). The potential for damage caused by earthquakes, volcanic eruptions, and tsunamis is exceptionally high across a great deal of the state.

Geological and tectonic interest in Alaska as well as the natural hazards, have motivated a rapid expansion of seismic instrumentation across the state, including the recently deployed EarthScope USArray Transportable Array (TA). These data now present the unprecedented opportunity to model the earth's crust and mantle beneath Alaska in much greater detail.

Existing studies of the crust and mantle beneath Alaska have been based on a variety of types of data and approaches, including seismic refraction and reflection profiling (e.g., Fuis et al., 1995, 2008), receiver function analyses (e.g., Ferris et al., 2003; Rondenay et al., 2010; O'Driscoll and Miller, 2015; Miller & Moresi, 2018; Miller et al., 2018; Zhang et al., 2019), body wave tomography for isotropic and anisotropic structures (e.g., Zhao et al;, 1995; Eberhart-Phillips et al., 2006; Tian and Zhao, 2012; Martin-Short et al., 2016; Gou et al., 2019), shear wave splitting studies (e.g., Yang & Fischer, 1995; Wiemer et al., 1999; Christensen & Abers, 2010; Hanna & Long, 2012), ambient noise tomography (e.g., Ward, 2015), and earthquake surface wave tomography (e.g., Wang & Tape, 2014). Some studies combined multiple datasets. For example, Allam et al. (2017) used body wave double-difference tomography and receiver functions to infer crustal and mantle structures along the Denali fault system. Ward & Lin (2018) performed a joint inversion of ambient noise surface waves and receiver functions to constrain shear wave speeds beneath Alaska. Jiang et al. (2018) used the ambient noise measurements from Ward and Lin (2018) and introduced longer period measurements from earthquakes and S-wave travel time residuals to construct an isotropic Vs model of the crust and upper mantle. Similarly, Martin-Short et al. (2018) present results of a joint inversion of ambient noise, earthquake-based surface waves, P-S receiver functions, and teleseismic S-wave travel times.

The purpose of this study is to construct a 3-D model of apparent radial anisotropy of shear wave speeds (Vsv, Vsh) in the crust and upper mantle beneath Alaska using surface wave observations. The model is based on data recorded by the TA as well as other permanent and temporary networks in and around Alaska (**Fig. 1b**). To achieve this purpose, we perform surface wave ambient noise tomography across Alaska as well as earthquake tomography, which extends dispersion measurements to longer periods. The resulting Rayleigh wave dispersion curves run from 8 to 85 s period and Love wave curves from 8 to 50 s. The model may serve usefully as the basis for earthquake location and source characterization, and to predict other types of geophysical data (e.g., body wave travel times, gravity, perhaps mantle temperature). It may also serve as the basis for wavefield simulations (e.g., Feng and Ritzwoller, 2017), and radial anisotropy provides information about crustal and mantle deformation (e.g., Moschetti et al., 2010; Xie et al., 2013). It is also designed to provide a starting point for further studies that introduce complementary datasets (e.g., receiver functions, Rayleigh wave H/V ratio, Rayleigh wave azimuthal anisotropy, body waves, shear wave splitting, and so forth) to refine the model. Such refinements may result in better determination of shallower structures and internal interfaces within the Earth (e.g., Shen & Ritzwoller, 2016), as well as estimates of the full depth-dependent elastic tensor in the crust and mantle (e.g., Xie et al., 2015, 2017). Within a Bayesian Monte Carlo framework (e.g., Shen et al., 2013), we strive to provide reliable information about model uncertainties across the region of study, which will help guide the future use of the model.

The principal novelty of this study lies in the simultaneous interpretation of Rayleigh and Love wave data. By measuring dispersion curves from both types of surface waves we are able to present the first model of Vsh as well as Vsv for the Alaskan crust and uppermost mantle. This results in the estimation of apparent radial anisotropy, about which we say more directly below. There are three other noteworthy characteristics of the study. (1) We include data through February 2019, which improves data coverage, particularly for the Brooks Range and the Alaska North Slope, and the model extends over a larger region than many earlier studies. (2) By employing earthquake data, the resulting surface wave data set is broad band, extending from 8 s up to 85 s period, which allows simultaneous constraints to be placed on structures in the mantle and in the shallow crust. (3) We estimate model uncertainties, which guides the assessment and interpretation of the resulting 3D model.

In discussing anisotropy using surface waves, it is useful to bear in mind two coordinate systems. The first is the frame defined by a symmetry axis (or foliation plane) of the medium of transport, in which "inherent" anisotropy is defined, and the second is the frame of the observations where "apparent" anisotropy is defined. We follow Xie et al. (2017) and refer to measurements of anisotropy and inferences drawn from them in the observational frame as "apparent". Apparent S-wave radial anisotropy, also referred to as polarization anisotropy, is the difference in propagation speed between horizontally (Vsh) and vertically polarized (Vsv) S-waves, where Vsh and Vsv are properties of the medium defined in the observational frame. A common measure of the strength of apparent S-wave radial anisotropy is the Thomsen parameter (Thomsen, 1986; Xie et al., 2017), γ, which is approximated by

$$\gamma = \frac{V_{sh} - V_{sv}}{V_{sv}}. \tag{1}$$

γ is inferred by simultaneously interpreting Rayleigh waves, which are dominantly sensitive to Vsv, and Love waves, which are exclusively sensitive to Vsh. Without introducing apparent radial anisotropy, Rayleigh and Love wave dispersion curves commonly cannot be fit simultaneously, a phenomenon often referred to as the "Rayleigh-Love discrepancy". Hereafter, whenever we refer to "radial anisotropy", we will mean apparent S-wave radial anisotropy.

Most studies of anisotropy, including this paper, report measurements and models of particular aspects of apparent anisotropy. In contrast, Xie et al. (2015, 2017) present methods that use observations of apparent radial and azimuthal anisotropy to infer characteristics of the depth-dependent elastic tensor, which possesses information about inherent anisotropy. In this study, we do not present azimuthal anisotropy, therefore the inference of inherent anisotropy is beyond the scope of this paper.

Strong radial anisotropy is a common mantle property (e.g., Montagner and Tanimoto, 1991; Ekstrom and Dziewonski, 1998; Shapiro and Ritzwoller, 2002; Marone et al., 2007; Kustowski et al., 2008; Nettles and Dziewonski, 2008; Yuan et al., 2011). This is often interpreted to result from the lattice preferred orientation (LPO) of olivine, which is approximately an orthorhombic mineral, and develops due to strain caused by plate motions. In a number of regions around the earth (e.g., Tibet, western US), strong crustal radial anisotropy has been found to coincide with extensional provinces (e.g., Moschetti et al., 2010; Xie et al., 2013), and this anisotropy is presumed to be caused by the LPO of crustal minerals, notably micas, whose foliation plane orients sub-horizontally under significant horizontal strain. Thus, observations of apparent radial anisotropy provide qualitative information about the deformation state of the crust or upper mantle. In the long run, however, it may be worthwhile to consider observations of apparent radial anisotropy as a stepping stone to more complete estimates of the elastic tensor and inference of inherent anisotropy, as performed by Xie et al., (2015, 2017). In addition, we discuss radial anisotropy in the North Slope Foreland Basin, or Colville Basin (Bird and Molenaar, 1992), which is the largest basin in Alaska.

The paper is organized as follows. In section 2 we present information about the data sets and the tomographic methods used in this study, including how we estimate uncertainties. Section 3 presents the 2-D phase and group speed maps along with corresponding uncertainties, and section 4 shows how the shear wave speed model (Vsv and Vsh) is produced by a Bayesian Monte Carlo inversion given dispersion data and uncertainties extracted from the tomographic maps. We present the features revealed by the model in section 5 and discuss them in section 6.

2. Data, Tomographic Methods, and Uncertainty Estimation

2.1 Data

This study utilizes seismic records from 22 permanent and temporary networks deployed across Alaska and northwest Canada between January 2001 and February 2019 (**Fig. 1b**). There are 537 seismic stations in total. Network names are listed in **Table 2**. Among those networks, the largest are the Transportable Array (TA) and the Alaska Regional Network (AK), which consist of 198 and 112 stations, respectively, and together compose nearly 60% of the stations used.

We perform ambient noise data processing by following the procedures described by Bensen et al. (2007), Lin et al. (2008), and Ritzwoller and Feng (2019). The Rayleigh wave is retrieved from the vertical-vertical (ZZ) component of the noise correlations while the Love wave is obtained from the transverse-transverse (TT) component. We then measure Rayleigh wave phase and group speeds between 8 and 60 s period and Love wave phase speed between 8 and 50 s period across the entire study region using automated frequency-time analysis. Additionally, we obtain broadband waveforms from teleseismic earthquakes with Ms > 5.0 (about 1,500 events), from which we obtain Rayleigh wave phase speed measurements from 30 to 85 s period and Love wave phase speed measurements from 30 to 50 s period to complement and augment the ambient noise data base.

2.2 Tomographic methods

Where the distribution of stations is relatively dense and regular, we are able to perform eikonal tomography (Lin et al., 2009), a geometrical ray theoretical method, to produce phase speed maps from ambient noise dispersion data. Eikonal tomography results in local observations of phase speed and uncertainty versus the azimuth of propagation, as exemplified by **Figure 2**. For each grid point and period where eikonal tomography is performed, phase speed measurements are averaged in 18-degree azimuthal bins, and the standard deviation of the mean, σ_i , is computed for the measurements in each azimuthal bin i. The isotropic phase speed measurement for the grid point is the weighted average of the bin-averages, where the weights are the reciprocals of the σ_i. The standard deviation of the isotropic phase speed is the mean of the bin standard deviations divided by the square root of the number of bins. Interpretation of the azimuthal variation of the measurements is beyond the scope of this paper.

The region where eikonal tomography has been applied is encircled with black dashed lines in **Figures 3a-c** and **4a-c** for Rayleigh and Love wave phase speeds, respectively. Elsewhere, where eikonal tomography is inapplicable, we apply a great-circle (or straight-ray) tomographic method (Barmin et al., 2001), which extends the region of coverage substantially. The straight ray method is applied across the entire region of study to construct the Rayleigh wave group speed maps (**Fig. 3d-f**). The group speed measurements help to improve constraints on the shallower parts of the earth structure. We do not use Love wave group speed data because of lower quality. We also apply eikonal tomography to Rayleigh and Love wave earthquake travel time measurements to extend phase speed maps to longer periods. We find that the impact of Helmholtz tomography (Lin & Ritzwoller, 2011), which models finite frequency effects on the long period surface wave maps, is small compared with the uncertainties of the maps. Therefore, here we do not apply the finite frequency corrections.

Comparisons of straight ray tomographic to eikonal tomographic maps have been presented by Lin et al. (2009) and Shen et al. (2016). There is typically a small mean difference caused by the fact that eikonal tomography models off-great circle propagation, and maps constructed with that method are typically slightly slower than those based on great-circle rays. We see similar comparisons across Alaska. However, the two methods are consistent within the uncertainties of the maps, as long as the damping applied in the straight ray method is calibrated to match eikonal tomography in the region of overlap of the methods. Thus, straight ray tomography can be applied reliably to extend the coverage of the dispersion maps outside the zone of applicability of eikonal tomography.

In practice, we construct the finalized phase speed maps by combining the ambient noise and earthquake measurements rather than performing tomography for each data set separately and then combining the dispersion maps. For Rayleigh waves, from 8 – 28 s only ambient noise measurements are used, but from 30 – 60 s the phase speed maps are constructed by averaging the ambient noise and earthquake measurements. Finally, for periods above 60 s, only earthquake measurements are used. For Love waves, from 8 – 28 s only the ambient noise data set is used, but from 30 – 50 s the phase speed maps are constructed using both ambient noise and earthquake measurements. The combination of the two types of measurements (ambient noise and earthquake travel times) enhances the quality of the tomographic maps when both types of measurements are available and is motivated by the fact that the maps produced from ambient noise or earthquake data alone are consistent, as illustrated by Ritzwoller et al. (2011).

2.3 **Uncertainty estimates**

As discussed in section 2.2, eikonal tomography produces uncertainty estimates where it is performed for phase speed. This approach does not estimate systematic errors or account for the correlation of errors in different travel time measurements. Therefore, as suggested by Lin et al. (2009), we multiply the error estimate from eikonal tomography by a factor of 2.0, which provides a more realistic estimate of uncertainty at each point on a phase speed map.

In the peripheral parts of the study region, where eikonal tomography cannot be performed, the maps derive from straight ray tomography (Barmin et al., 2001), which does not produce estimates of uncertainty but does provide resolution estimates. Similar to Shen et al. (2016), we infer uncertainties in these regions from resolution by applying an empirical scaling relationship that transforms resolution (in km) to uncertainty (in m/s) using the following formula:

$$\sigma(\vec{r}) = kR(\vec{r}) \qquad (2)$$

where $\sigma(\vec{r})$ is the uncertainty estimate at location $\vec{r}$ where eikonal tomography has not been performed, and $R(\vec{r})$ is the estimate of resolution, which is the standard deviation of the resolving kernel at the location (Barmin et al., 2001). We estimate the value of k in equation (2) for each period separately at the grid points where both the eikonal and straight ray tomographic results are available. Typical values of k are ~ $0.2 \times 10^{-3}\ \mathrm{s}^{-1}$, so that a 50 km resolution produces an uncertainty estimate of about 10 m/s.

Because we construct group speed maps with straight ray tomography, we must scale resolution to uncertainty everywhere. Uncertainties for group speed maps are also computed from equation (2), but we multiply k (determined for phase speed at that period) by a factor of 2.0, which amplifies group speed uncertainties by a factor consistent with relative data misfit found in constructing the dispersion maps. Absolute residuals for group speed measurements are typically about twice as large as phase speed residuals.

Spatially averaged uncertainties for Rayleigh and Love phase speeds, taken from the uncertainty maps, are shown in **Figure 5**. The spatial distribution of the uncertainties is quite homogeneous in the interior of the region of study, but degrades in a systematic way near the periphery. Rayleigh and Love wave phase speed uncertainties average about 20-30 m/s, but grow at the shorter and longer periods. Rayleigh wave group speed uncertainties tend to be about twice as large. The uncertainty in the difference between Love and Rayleigh wave speeds is about the square-root of 2 times larger than uncertainties in either wave type. Love wave phase speed uncertainties grow to be larger than the Rayleigh wave uncertainties above 30 s period where earthquake data are introduced because more earthquakes produce high-quality phase time measurements for Rayleigh waves than for Love waves.

3. Tomographic Maps

Examples of Rayleigh wave phase and group speed maps are presented in **Figure 3**. At 10 s period (**Fig. 3a,d**), the Rayleigh wave is most sensitive to the uppermost crust including sedimentary basins. Several sedimentary basins, including the North Slope foreland basin, which we call the Colville basin, as well as several smaller basins are captured in the group speed map. Because group speed at each period has a shallower sensitivity than phase speed, the 20 s group speed map (**Fig. 3e**) is qualitatively quite similar to the 10 s phase speed map (**Fig. 3a**). The black contour on the 10 s group speed map (**Fig. 3d**) identifies the Colville basin and is used later in the paper. The 40 s group speed (**Fig. 3f**) strongly reflects changes in crustal thickness, where lower wave speeds indicate deeper crust. The high velocity anomaly located in the northeast corner of the 40 and 70 s period Rayleigh wave phase speed maps (**Fig. 3b, c**) identifies the North American craton. At 70 s, there are high velocity anomalies associated with the subducting Pacific slab and the Arctic Alaska craton.

Figure 4a-c presents examples of Love wave phase speed maps at periods of 10, 20 and 40 s. Love waves sample somewhat more shallowly than Rayleigh waves at the same period, so it is not surprising that the 20 s Love wave phase speed map is qualitatively similar to the Rayleigh wave map at 10 s period.

We also present the differences in phase speed between Love and Rayleigh waves in **Figure 4d-f**. The white contours identify the regions where the Love wave is slower than the Rayleigh wave, which is a consequence of the existence of a water layer and thick sediments. Fitting the difference between Rayleigh and Love wave velocities is one of the primary goals of a model of apparent radial anisotropy.

4. Constructing the 3-D Model

Local Rayleigh wave phase and group speed and Love phase speed curves with uncertainties are taken directly from the associated dispersion and uncertainty maps on a spatial grid with a 1.0° spacing in longitude and 0.5° spacing in latitude, resulting on average in about a 50 km grid spacing. Dispersion curves with uncertainties presented as error bars are shown for four example locations (Brooks Range, Yukon Composite Terrane, the Alaska subduction zone Back-Arc, and the Cook Inlet) in Alaska in **Figure 6**. These locations are identified with yellow stars in **Figure 1a**. Typically, Love wave phase speed is greater than Rayleigh wave phase speed at the same period, but there are exceptions in wet regions at short periods (e.g., Cook Inlet, **Fig. 6d**).

The local surface wave dispersion curves are the input for the Bayesian Monte Carlo inversion that produces a posterior distribution of vertical shear wave speed (Vsv, Vsh) profiles that predict the dispersion data acceptably. We closely follow the inversion procedure described by Shen et al. (2016), which consists of three steps.

(1) The first step is to construct the prior distribution of models on the 50 km grid. The prior distribution is controlled by the model parametrization, the reference model, and constraints on each model parameter. The range of the model variables is typically broad enough that an ensemble of models with acceptable data fits can be found.

(2) The second step is the Monte Carlo sampling of model space and determining data misfit. Based on the Metropolis algorithm (Mosegaard & Tarantola, 1995), we perform a series of random walks in model space that select a chain of candidate models in the prior distribution. For each individual model selected in the random walk, theoretical Rayleigh wave phase and group speed and Love wave phase speed curves are computed using the transversely isotropic forward code of Robert Herrmann's Computer Programs in Seismology (Herrmann, 2013) with earth flattening, and the misfit to the data at each point is calculated. Data misfit is defined as follows:

$$\chi = \sqrt{\frac{1}{N}\sum_{i=1}^{N}\frac{(d_i - p_i)^2}{\sigma_i^2}} \quad (3)$$

where d_i is an observed datum (Rayleigh wave phase or group speed or Love wave phase speed), p_i is that data value predicted from a given model, and σ_i is the one standard deviation data uncertainty. The index i ranges over dispersion data, where N is the number of the data values. A chain of candidate models terminates when sufficient steps have been taken to reach an equilibrium in model space and misfit. Then, the inversion starts afresh at a random point in the prior distribution with a new chain and the procedure is repeated on the order of 300 times.

(3) The third step is to construct the posterior distribution. After the second step terminates at each grid point, the model with the best data fit is identified as the "best fitting model" with misfit $\chi_{\min}$ and the "mean model" ($\bar{m}$) is defined as the mean of the ensemble of accepted models at each depth and for each discontinuity. Examples of average models at two locations are shown in **Figure 7**. A model is accepted if the misfit is less than $\chi_{\min} + 0.5$, where $\chi_{\min}$ is the misfit value for the best fitting model.

4.1 Model parametrization

The models we consider are essentially depth-dependent distributions of Vsv and Vsh, with Vp and density scaled to Vsv. Vsh and Vsv are related through equation (1), and we consider the shear wave speed part of the model specified by Vsv and γ, where $Vsh = (1+\gamma)Vsv$. We set Vph = Vpv and η = 1, which is physically unrealistic because Vs anisotropy would be accompanied by Vp anisotropy with η ≠ 1 (e.g., Babuška and Cara, 1991; Erdman et al., 2013). However, as Xie et al. (2013) have shown, the effect of this assumption on estimates of Vs radial anisotropy is negligible.

Each vertical profile on the ~50 km spatial grid across the study region consists of a vertical stratification of three categories of structure: the sediments, the crystalline crust, and the upper mantle. The first category is the sedimentary basin, which is represented by three model parameters: thickness and Vsv at the top and bottom of the sediments. The Vsv values in the sediments increase linearly from the top to the bottom. We assume that the sediments are isotropic, so that Vsv=Vsh, except in the Colville Basin where it is necessary to introduce non-zero sedimentary anisotropy, γ_s. The second category is the crystalline crust, which is described by thickness (from the base of the sediments to Moho), four cubic B-splines with variable coefficients, and the intensity of crustal radial anisotropy, γ_c, which is non-zero outside the Colville Basin. The third category is the mantle. Vsv from the Moho to 200 km depth is determined with five cubic B-splines, while Vsh is found from γ_m which is constant with depth. For offshore locations, an additional water layer is added to the top of the model, with water layer thickness determined from the ETOPO-1 model (Amante & Eakins, 2009) and Vsv = Vsh = 0 km/s, Vp = 1.5 km/s, and density = 1.02 g/cm^3.

Once a Vsv model is constructed for testing, Vp is computed using Vp/Vsv = 2.0 in the sediments and Vp/Vsv = 1.75 in the crystalline crust and mantle. The density in the crust is determined from Vsv and Vp with the empirical relationship presented by Brocher (2005). In the mantle, however, density is scaled from Vsv perturbations relative to 4.5 km/s with 10 kg/m^3 per 1 % velocity change following Hacker and Abers (2004).

We assume that radial anisotropy is vertically constant and non-zero in the mantle, γ_m. In the crust, our parameterization of anisotropy depends on sedimentary thickness because in regions with very thick sediments we are unable to estimate radial anisotropy reliably in the crystalline crust. The Colville Basin, identified by the dark blue contour in **Figure 3d**, is the region where the impact from the sediments on the estimation of crustal anisotropy is the most profound. Therefore, in the Colville Basin we allow there to be sedimentary anisotropy but no crustal anisotropy ($\gamma_s \neq 0, \gamma_c = 0$), and consider crustal anisotropy to be indeterminate. In regions outside the Colville Basin, we set sedimentary anisotropy to zero but allow anisotropy in the crystalline crust ($\gamma_s = 0, \gamma_c \neq 0$).

The result is that the anisotropic part of the model is fully described by two different values of γ everywhere, one for the crust (γ_s or γ_c) and the other for the mantle (γ_m). As we show in section 5.2.1, this simple parameterization in which the amplitude of radial anisotropy is constant either in the sediments or the crystalline crust and also in the upper mantle is sufficient to fit the data across the study region. However, this parameterization differs from the study of Xie et al. (2013), which found that substantial depth-variability of the strength of radial anisotropy was needed to fit the data in Tibet.

The shear Q values in the crust are fixed to the values in the ak135 model; namely, Q = 80 in the sediments and Q = 600 in the crystalline crust. With these values, there is little physical dispersion in the crustal shear modulus. Shear Q is fixed at 150 in the mantle for simplicity, which is similar to the choice by Shen & Ritzwoller (2016).

The resulting parameterization consists of 15 unknowns for each grid point: two for the sediments (Vsv), one for sediment thickness, four for the crystalline crust (Vsv), one for crustal thickness, five for the mantle (Vsv), and two for apparent radial anisotropy in order to find Vsh in the mantle and either the crystalline crust or sediments; i.e., either (γ_c, γ_m) or (γ_s, γ_m).

4.2 Prior distributions

The prior distribution used in the inversion involves variations around a reference model, which is a combination of the 1-D model ak135 (Kennett et al., 1995) with the 3-D CRUST-1.0 (Laske et al., 2013) model. The sedimentary and crustal thicknesses in the reference model are from CRUST-1.0, while the shear wave speeds in the crust and mantle are from ak135. The prior distribution defines a range of models around the reference model, where the range is determined from the parameterization of the model and the imposed constraints. The constraints we impose are of two types.

The first type of constraint is the allowed range of perturbations to the reference at each location, which prescribes the extent of model space explored in the Monte Carlo sampling. The allowed ranges on the 15 variables that define the 3-D model at each point are summarized in **Table 3**. For example, we allow there to be $\pm$ 50% perturbations around the reference model for crustal thickness, and $\pm$ 20% for the B-spline coefficients in the crust and mantle. We also allow sedimentary thickness to vary from 0 to twice the input thickness from CRUST-1.0, and large changes to Vsv in the sediments. Radial anisotropy in the crystalline crust, γ_c, and in the mantle, γ_m, range separately from $\pm$ 10%, although beneath the Colville Basin $\gamma_c = 0$. Sedimentary anisotropy, γ_s, beneath the Colville Basin can range from 0 to 25%, but is zero outside this basin. The result is that there are very large bounds considered around the reference model for the location of interfaces, shear wave speeds, and values for apparent radial anisotropy.

The second type of constraint involves explicit bounds imposed on aspects of each vertical model profile considered. There are eight prior constraints imposed in constructing candidate models allowed in the prior distribution. If a model profile is constructed that violates one of these constraints, it is rejected prior to computing data fit. (1) At jump continuities (base of the sediments, Moho), the jump is positive with depth for both Vsv and Vsh. (2) Both Vsv and Vsh in the crust are less than 4.3 km/sec at all depths. (3) Both Vsv and Vsh increase monotonically with depth in the crust, which we refer to this as the “monotonicity constraint”. (4) At the top of the mantle, Vsv and Vsh are both less than 4.6 km/sec and greater than 4.0 km/sec. (5) At the bottom of the model, i.e., at 200 km depth, Vsv and Vsh both are greater than 4.3 km/sec. (6) Both Vsv and Vsh at all depths (0 – 200 km) are less than 4.9 km/sec. (7) Vsv and Vsh are both greater than 4.0 km/sec for depths below 80 km. (8) The difference at internal maxima and minima in Vsv in the mantle is less than 10 m/s. Together these constraints act to discourage vertical oscillations in the crust and mantle, as well as large non-physical excursions, and are hypotheses that we are testing. We should only infer a more complicated model if we cannot fit the data with these constraints in place.

Examples of prior distributions for several locations are shown with white histograms in **Figure 8**. The prior distributions of crustal and mantle radial anisotropy are nearly uniform, because there are no additional constraints applied to the them. The prior distributions for crustal thickness have a slight preference for smaller values, due to the monotonicity constraint (which ensures larger values of Vs deeper in the crust). The monotonicity constraint also tends to skew the prior distributions for Vsv and Vsh at 15 km and 100 km.

4.3 Posterior distributions

Posterior distributions of models are constructed based on data fit by the models chosen in the Monte Carlo sampling of model space, and reflect how well model characteristics are constrained by the data. As discussed earlier, a model is accepted into the posterior distribution if its misfit χ is less than $\chi_{\min} + 0.5$, where $\chi_{\min}$ is the misfit value for the best fitting model. The mean and standard deviation of the posterior distribution define the 3-D model (termed the mean model, $\bar{m}$) and the uncertainty estimates (σ_m). As argued by Shen and Ritzwoller (2016), σ_m is too large to provide a reasonable estimate of uncertainty, but does reflect relative uncertainty, which is useful to assess how well shear wave speeds and topography on internal interfaces are constrained by the data set.

Figure 7 shows examples of the mean model at two locations: beneath the Brooks Range where crustal anisotropy is non-zero and beneath the Colville Basin where sedimentary anisotropy is non-zero. These profiles illustrate that the resulting models are smooth in the crust and mantle, are monotonically increasing in the crust, have positive jumps in both Vsv and Vsh at the two discontinuities, and have depth-variable apparent radial anisotropy which is, however, constant in the mantle and sediments or crystalline crust.

Examples of marginal posterior distributions for the same four grid locations shown for the prior distributions are presented with the red histograms in **Figure 8**. These posterior distributions reveal that Vsv in the interior of the crust and mantle are relatively well constrained. In contrast, near the boundaries of the crust the posterior distribution widens. This is illustrated in **Figure 9**, which shows the standard deviation of the posterior distribution averaged over the study region as a function of depth. In the interior of the crust and in the mantle between depths of about 50 and 100 km, the standard deviation of the posterior distribution is about 50 m/s. Near the boundaries in the crust the value more than doubles, and then it grows slowly at depths greater than 100 km. For this reason, we truncate the model and discuss its properties only to a depth of

120 km. **Figure 8** also shows that the posterior marginal distribution for crustal thickness is quite wide. Indeed, with surface wave data alone, internal interfaces in the Earth are typically poorly determined (e.g., Shen et al., 2016). The posterior distributions also indicate that crustal radial anisotropy, γ_c, tends to be better constrained than mantle radial anisotropy, γ_m.

Similar to Moschetti et al. (2010), we find that there is a trade-off between the values of radial anisotropy in the crust and mantle. As **Figure 10** illustrates, mantle radial anisotropy changes appreciably with changes in crustal radial anisotropy. At some locations, mantle radial anisotropy may not be required to fit the data, as illustrated by the points for the Brooks Range and the Cook Inlet in the marginal distributions of **Figure 8**, but at most locations crustal or sedimentary anisotropy is needed. We discuss this further in section 6.

5. Results

As described above, the mean model at each grid point ($\bar{m}$) as a function of depth and for the depth to each interface is mean of the posterior distribution, which defines the 3-D Vsv model as well as the amplitude of radial anisotropy in the crust (γ_c) or sediments (γ_s) and the mantle (γ_m). The standard deviation of the posterior distribution (σ_m) provides a conservative estimate of uncertainty (e.g., Shen and Ritzwoller, 2016). Here, we discuss the characteristics of the 3-D model for isotropic structure and radial anisotropy.

5.1 3-D isotropic model: Vsv

Figure 11a shows the sedimentary thickness estimates of the mean model. Clearly, the Colville Basin in the Alaskan north slope region is the most significant basin, but other basins are also resolved in the model and are labeled with numbers in **Figure 11a** and identified in **Table 4.** Sedimentary thickness is quite uncertain due to the trade-off with upper crustal shear-wave speeds. Shear wave speed at the top of the crystalline crust is also affected by this trade-off, as the uncertainties in **Figure 9** illustrate.

The shear wave speed distribution (Vsv) averaged from the surface of the Earth to a depth of 6 km is presented in **Figure 11b**. This depth-range also displays the imprint of the basins where they exist, but where basins do not exist it provides an estimate of crustal wave speed in the upper crystalline crust. This figure and those at other depths present slices over a similar depth range (±3 km).

In the middle crust, near 20 km depth (**Fig. 11c**), the model is better determined than nearer to the surface, due to fewer trade-offs away from interfaces. However, uncertainty increases dramatically when Moho depth approaches 20 km, which it does near the southern edge of the study region. There is a prominent low velocity lineation running near the major faults bounding the Brooks Range. A low velocity anomaly at this depth also appears near the Chugach-Prince William terrane, in the middle of the Yakutat microplate which is identified by the white polygon in the figure, and near the Wrangell volcanic field. High velocity anomalies are observed in the crust above the subducting Alaska-Aleutian slab and beneath the North American craton.

Near the bottom of the crust (**Fig. 11d**), the lateral variability of Vsv is weaker, except for small regions off-shore where the crust is thinner than on the continent. Lowest velocities (3.70 – 3.75 km/s) onshore run near the major faults bounding the Brooks Range, as they do at 20 km depth, and in the Wrangell volcanic field. The highest velocities (above 3.95 km/s) are found in the interior of the state and in Arctic-Alaska and the North American craton in northern Canada. Uncertainty increases in the lowermost crust because of trade-offs with Moho depth, as **Figure 9** shows.

Crustal thickness estimates are presented in **Figure 12a** and one standard deviation of the posterior distribution in **Figure 12b**. Crustal thickness is typically poorly constrained by surface wave dispersion data alone, and uncertainties are fairly uniform geographically, averaging about 4 – 5 km. Nevertheless, our crustal thickness estimates differ substantially from the reference model **(Fig. 12c),** but are similar to those of Miller & Moresi (2018) based on receiver functions (**Fig. 12d)**. Details differ but the large-scale features are similar. Notably, and unsurprisingly, the crust is thicker beneath the Brooks Range and the Alaska Range while it is thinner in the interior of Alaska; e.g., the Yukon Composite Terrane. **Figure 13** shows a histogram of differences between our model and that of Miller & Moresi (2018), where the mean difference is about 1.5 km (Moho in our model is on average a bit shallower) and the standard deviation of differences is about 3.4 km. Thus, the mean difference between the models is within one standard deviation of the posterior distribution, presented in **Figure 12b.**

Two horizontal Vsv slices of the mean model are shown in **Figure 14** at depths of 60 km and at 100 km in the mantle. The most prominent positive anomalies are the cratonic roots beneath Artic-Alaska and the North American craton. The edge of the velocity anomaly in Canada forms the so-called Cordillera-Craton boundary. In the interior of Alaska, the mantle is mostly a broad relative low velocity zone. High topography of the Brooks Range, the Alaska Range, and other ranges are not underlain uniformly by low velocity uppermost mantle, which has implications for the nature and depth extent of isostasy (e.g., Levandowski et al., 2014). The Wrangell volcanic field at 60 km is underlain by low velocities in the mantle, particularly offset north of the volcanoes. The back-arc area northwest of the Alaska-Aleutian subduction zone displays low velocity features in the supra-slab wedge that encompass the volcanoes at 60 km depth but which is offset further to the northwest at greater depths. Subducting lithosphere is imaged clearly at 100 km, but at 60 km it is mainly offshore along the Alaska-Aleutian subduction zone and not as well resolved. The nature of subducting lithosphere in the 3-D model is discussed in greater detail in section 6.

5.2 3D model of radial anisotropy: γ_c, γ_m

5.2.1 Data fit as a function of model parameterization

Data misfit, defined by equation (3), for various models is shown in **Figure 15**. For the data to be considered fit well, a value of misfit below about 2.0 should be achieved. **Figure 15a** shows the misfit for the isotropic model, in which Vsh = Vsv so that $\gamma_s = \gamma_c = \gamma_m = 0$. This map reveals the Rayleigh-Love discrepancy. Across most of Alaska the Rayleigh and Love wave dispersion data cannot be fit simultaneously with an isotropic model, and average misfit (eqn. (3)) is 2.41.

As discussed in section 4.3, there is a substantial trade-off between crustal and mantle anisotropy that broadens the posterior distribution for both γ_c and γ_m, but reliable simultaneous estimates of these variables are possible in most places. However, due to the exceptionally large anisotropy, γ_s, in the Colville Basin we cannot estimate γ_c reliably. In this basin, we allow anisotropy in the sediments and mantle but not in the crystalline crust (i.e., $\gamma_c = 0, \gamma_s \neq 0 \neq \gamma_m$), but outside the basin the model includes anisotropy in the crystalline crust and mantle but not the sediments (i.e., $\gamma_s = 0, \gamma_c \neq 0 \neq \gamma_m$). The resulting data misfit is shown in **Figure 15b**. With the model including mantle and crustal (or sedimentary) radial anisotropy, the data can be fit across the entire region of study with an average misfit of 0.78.

Without sedimentary or crystalline crustal anisotropy but including mantle anisotropy ($\gamma_s = \gamma_c = 0, \gamma_m \neq 0$), the misfit is shown in **Figure 15c**. The average misfit is 1.40, and across much of Alaska there is a large residual misfit, particularly in the parts of the state north of the Denali fault. This includes the Colville basin, as well as the area along the Brooks Range and the region between the Denali and Tintina faults focused broadly on the Yukon Composite Terrane. Thus, to achieve acceptable data fit, crustal anisotropy must be introduced in the crystalline crust or the sediments of the Colville Basin. **Figure 15d** presents the misfit from the inversion that includes sedimentary or crustal anisotropy but not mantle anisotropy (i.e., $\gamma_m = 0, \gamma_s \neq 0$ or $\gamma_c \neq 0$). The misfit value drops dramatically when introducing crustal anisotropy (from 1.40 to 0.78) and increases only moderately when turning off mantle anisotropy (from 0.78 to 0.95). Thus, the primary factor that determines data fit is actually crustal anisotropy (and in Colville Basin sedimentary anisotropy). Mantle anisotropy can be determined reliably even though its effect on the Rayleigh-Love discrepancy is weaker.

Figure 16 illustrates in greater detail the improvement in fitting the Rayleigh-Love discrepancy. The error bars in this figure are for differences in observed Love wave phase speed and Rayleigh wave phase speed at four locations for our final model ($\gamma_m \neq 0, \gamma_c \neq 0$ or $\gamma_s \neq 0$). The dashed line indicates the fit to this difference based on the isotropic model at each location, where Vsv = Vsh ($\gamma_s = \gamma_c = \gamma_m = 0$). There are large period-dependent discrepancies between the line predicted by the isotropic model and the observations. Beneath the Brooks Range and Cook Inlet, the discrepancy is approximately constant across period, implying that radial anisotropy is probably about the same in both the crust and mantle. In contrast, in the Aleutian Back-Arc region the discrepancy is larger at longer periods so that mantle anisotropy is probably stronger than crustal anisotropy, and in the Yukon Composite Terrane the discrepancy is greater at shorter periods indicating that crustal anisotropy is probably larger than mantle anisotropy there. In each of these cases, introducing radial anisotropy that is constant with depth separately in the crust and mantle, allows the data to be fit well.

5.2.2 The model of apparent radial anisotropy

The resulting estimates of crustal and mantle anisotropy are shown in **Figure 17**. We consider estimates of γ_c to be indeterminate if the standard deviation of the posterior distribution for γ_c is greater than 1.0% or in the Colville Basin where we estimate γ_s rather than γ_c. Estimates of γ_m are considered indeterminate if the standard deviation of the posterior distribution is greater than 1.5%. γ_m has a weaker impact on the Rayleigh-Love discrepancy than γ_c, so we make the tolerance broader for mantle anisotropy than for crustal anisotropy.

Crustal anisotropy is on average stronger than mantle anisotropy and more geographically variable. Mantle anisotropy is somewhat more homogeneous than crustal anisotropy, and the patterns of crustal and mantle anisotropy are generally complementary. In this latter respect, crustal and mantle anisotropy may have formed in response to different episodes of tectonic strain. In particular, the geographical distribution of crustal anisotropy corresponds in part to areas of significant crustal extension, as discussed further in section 6.3.

6. Discussion

6.1 Radial anisotropy of the Colville Basin

The North Slope foreland basin, or the Colville Basin or trough, is a late Mesozoic and Cenozoic basin that runs from the Brooks Range in the south to the edge of the Beaufort Sea in the north (e.g., Bird and Molenaar, 1992). The basin is about 1000 km long and 50 to 350 km wide, and is by far the largest basin in the region of study. We approximate its extent with the 2.5 km/s contour on the 10 s Rayleigh wave group speed map (**Fig. 3d**).

As indicated by the Vsv and Vsh profiles shown for a point in the Colville Basin in **Figure 7b**, the radial anisotropy in the sediments of the basin is much stronger than across the crystalline crust. Values of sedimentary apparent radial anisotropy average in excess of 20 % throughout the basin, similar to the large values reported by Xie et al. (2013) for the Sichuan Basin. The stratification and layering found in sedimentary basins probably generate this strong radial anisotropy. Our model cannot provide information about the layering of structures in basins, but we are confident that the anisotropy (γ_s) in the Colville Basin is exceptionally strong, much stronger than either crustal or mantle radial anisotropy (γ_c,γ_m). Additional data, such as receiver functions or Rayleigh wave H/V ratio, which are more sensitive the shallowest parts of the Earth and also provide better constraints on sediment thickness, may help to improve sedimentary structures, helping to provide better information about sedimentary anisotropy.

6.2 Resolved subducted lithosphere

Resolving subducted lithosphere including accurately capturing the geometry of the subducting slab, its thickness, and the amplitude of velocities in the slab is very challenging for inversions based on surface wave data alone for the following reasons. (1) Surface waves in general have better depth resolution than horizontal resolution. Consequently, the ability to determine lithospheric thickness varies with the dip angle of the slab. Slab thickness is better constrained when the lithosphere is horizontal, but as the dip angle increases the ability to determine slab thickness degrades appreciably. (2) A particular complication for our study is that a significant part of the Alaskan subduction zone is located at the southern edge of our model, which is offshore with poor path coverage for ambient noise data and no data coverage for earthquakes. Therefore, at least offshore, we lack dispersion measurements at the longer periods (indicated in **Fig. 3**), which reduces confidence in structures deeper than about 100 km. Shorter period dispersion measurements are also affected by reduced data coverage, which makes it harder to recover the amplitude of velocity anomalies correctly. Despite these issues, aspects of the subducting lithosphere at depths above about 100 km can be resolved reliably. In particular, we are able to resolve the top of the subducting slab above 100 km depth and its areal extent, especially in on-shore regions. **Figure 18** indicates some of these features.

To illuminate the well resolved features, we begin by comparing our 3-D Vsv model (mean of the posterior distribution) with two prominent slab models that delineate Alaskan subduction zones: Slab1.0 by Hayes et al. (2012) and the Alaska_3D 1.0 model by Jadamec & Billen (2010). These two models are generally consistent in depicting the Alaska-Aleutian subduction zone comprising dashed boxes A and B in **Figure 18**, which we call Blocks A and B. Slab edges from these model at 100 km depth are presented in this figure with the dashed red and solid cyan curves. However, unlike Slab1.0, the Alaska_3D 1.0 model also includes a slab kink near the Denali fault and the northern-most edge of the Denali volcanic gap, and the slab extends into what we refer to as the Yakutat subduction zone in Block C and beyond. Because our 3-D model also includes the slab kink (**Fig. 18**) near the Denali fault (Block B) and the subducting Yakutat slab (Block C) we will concentrate comparison of our model with Alaska_3D 1.0.

Following the cyan slab edge curve at 100 km depth from the west to the east in **Figure 18**, we divide the Alaskan subduction zone into four structurally distinct blocks: Blocks A - D. They are identified with letters in **Figure 18** as (A) the Aleutian subduction zone, (B) the Alaskan subduction zone and slab-edge or kink, which includes the Denali volcanic gap, (C) the Yakutat subduction zone, and (D) the Yakutat slab shoulder.

In the Aleutian subduction zone (Block A), the edge of the high velocity Pacific slab is consistent with the slab edge curves of both the Slab 1.0 and Alaska_3D 1.0 model. The location of the slab in our model also generally matches the locations of the Aleutian volcanic arc (white triangles) and earthquakes in the depth range near 100 km (yellow dots). We also note that there is an anomaly in slab structure (identified as Oval 1 in **Fig. 18**) located near the Barren Islands in the strait between the Kenai Peninsula and Kodiak Island. This is what we call the “Barren Islands slab anomaly”, which is a notable reduction in shear wave speed at 100 km depth and occurs in a region of heightened seismicity at this depth. Profile A-A’ in **Figure 19** extends across the Barren Islands anomaly and shows the anomaly in cross-section (black oval labeled with the number 1 in the A-A’ cross-section) as a reduction in shear wave speed in a confined depth range that occurs adjacent to very slow velocity supra-slab wedge in the back-arc. In contrast, profile B-B’ in **Figure 19** extends through a more normal section of the subducting lithosphere, in which no low velocity anomaly appears and the back-arc is not as slow. Yang & Gao (2019) also report a low velocity region in the uppermost mantle near the Barren Islands and refer to it as a “slab gap” characteristic of horizontal slab segmentation and perhaps a slab tear. In contrast, we image this as a vertically confined anomaly, so we do not refer to it as a gap and do not image a structure that is consistent with slab segmentation or a tear that extends across a significant depth range. Consequently, we hypothesize that the Barren Islands slab anomaly reflects slab heating caused by higher temperatures and perhaps fluid or melt in the back-arc region localized near 100 km depth. However, the Barren Islands slab anomaly may result from failing to recover the full amplitude of the positive anomaly within the slab. Further efforts are warranted to improve the vertical and horizontal resolution of this intriguing lithospheric feature in order to clarify its physical cause.

The Alaskan subduction zone ends northward to a slab edge or kink, which is identified as the edge of Block B in **Figure 18**. Rondenay et al. (2010) propose that the Denali Volcanic Gap is caused by the cooling effect of the Yakutat slab, which essentially reduces melt production and hinders magma ascent to the surface. We observe high shear wave speed lithosphere beneath the Denali Volcanic Gap region, consistent with Jiang et al. (2018) and Martin-Short et al. (2018). Others have argued that the kink structure may result in toroidal mantle flow around it, and the flow pattern predicted by the geodynamical model of Jadamec & Billen (2010) is consistent with SKS splitting studies (e.g., Christensen & Abers, 2010; Hanna & Long, 2012; Perttu et al., 2014).

Oval 2 located northeast of Block B in **Figure 18** is a high velocity extension to the slab edge, which was suggested to be an aseismic slab edge by Gou et al. (2019). This aseismic slab edge has also been imaged by Jiang et al. (2018).

Moving eastward along the slab edge from the slab kink to the Yakutat subduction zone, Block C in **Figure 18**, there is another relative low velocity anomaly (Oval 3) located northwest of the Wrangell Volcanic Field (Oval 4). This "Wrangellia slab anomaly", as we call it, is also captured by the Vp model of Gou et al. (2019) at a similar depth range. The vertical cross section C-C' in **Figure 19** shows that the high-speed anomaly in Block C appears to be part of the subducting Yakutat slab and occurs at the location of the slab in model Alaska_3D 1.0. Jiang et al. (2018) suggest that this part of the slab is sinking vertically because the subduction is slowed down by the Yakutat collision. The presence of this high-speed subducted lithosphere at a similar location is also reported by Martin-Short et al. (2018) and Gou et al. (2019).

As illustrated in **Figure 18**, there is an increasing mismatch in slab geometry between our model and Alaska_3D 1.0 as the edge of Yakutat slab extends southeastward into what we refer to as the "Yakutat slab shoulder" region (Block D). The corresponding vertical cross-section D-D' in **Figure 19** shows a high-speed anomaly seaward of the Chugach Mountains rather than near the slab edge predicted by the model Alaska_3D 1.0. This anomaly is separated from another high-speed anomaly identified by Oval 5 in D-D', which is in the slab shoulder region of the Yakutat slab. It is not clear whether this detachment indicates thickened lithosphere of the Yakutat terrane or the onset of subduction further south of what the Alaska_3D 1.0 model predicts. This high-speed Yakutat slab shoulder has not been reported in previous studies.

In closing, we note several features that appear in the vertical cross-sections that we do not feel justified interpreting. (1) The amplitudes of the high-speed anomalies weaken where the slab begins to subduct in cross-sections B-B' and C-C', marked with Ovals 6 and 7. This may be due to the difficulty in recovering amplitudes correctly due to poor data coverage at those locations, which reduces our confidence in these features. (2) The slab thickens and the slab edge increasingly mismatches the Alaska_3D 1.0 model below 100 km depth on vertical cross-sections A-A' and particularly B-B', which we believe are artifacts caused by degradation in resolution with depth. Introducing body wave datasets may potentially help better resolving the deeper part (>100 km) of the subduction zone, which is beyond the scope of this study. (3) Oval 8 in profile A-A' is an off-shore region where we are unable to resolve uppermost mantle structure reliably.

6.3 Extensional provinces and radial anisotropy

Crustal radial anisotropy (γ_c) averages about 2.6% in our 3-D model (**Fig. 17a**). It is strongest (> 2.6%) across a broad swath of central and northern Alaska, including the Seward Peninsula, the southern parts of Brooks Range, the Ruby Terrane, and the Yukon Composite Terrane, as shown in **Figure 20b**. Miller & Hudson (1991) identified regions in Alaska that were subjected to significant Cretaceous ductile extension, which they refer to as the "hinterland" of the Brooks Range fold and thrust belt. The regions they believe constitute the basement during the extensional episodes are shown schematically in **Figure 20a**. These extensional regimes are nearly coincident with the areas of strong crustal radial anisotropy that we image.

Crustal radial anisotropy also has been observed in other regions that have or are undergoing extensional deformation, including in Tibet (Shapiro et al., 2004; Xie et al., 2013) and the Basin and Range province of the western United States (Moschetti et al., 2010). The results we present here support the hypothesis developed in these earlier studies that deformation in the crystalline crust dominantly controls the formation of apparent radial anisotropy, and conversely that apparent radial anisotropy is a marker for crustal extension. Such anisotropy may result from the formation of middle to lower crustal sheet silicates (micas) with shallowly dipping foliation planes beneath extensional domains (e.g., Hacker et al., 2014). Xie et al. (2017) propose that the depth range of the deformation that is causing apparent radial anisotropy lies in the middle to lower crust, but we do not have the depth resolution to test this hypothesis.

6.4 Cratons and thickened lithosphere

The horizontal profiles of **Figure 14** illustrate similarity between the uppermost mantle beneath Arctic-Alaska and the North American (or Laurentian) craton to the east. Both appear as very high velocity features that extend at least to 120 km depth (e.g., **Fig. 21**, profile E-E') and presumably deeper, although we are unable to resolve features reliably below 120 km. Thus, the seismic evidence is quite clear that Arctic-Alaska appears to be underlain by very thick lithosphere that is possibly cratonic in nature.

Moore and Box (2016) describe several prominent models for the tectonic origin of Arctic-Alaska and the arrangement of terranes. These models include those in which Arctic-Alaska has maintained a fixed position relative to North America throughout Phanerozoic time and those they describe as more popular models that involve a large-scale counter-clockwise rotation and transport of Arctic-Alaska as part of the rotational opening of the Canada Basin in the Early Cretaceous. Kinematic models of the tectonic formation of Arctic-Alaska should consider that this region is underlain by very thick lithosphere that could inhibit large-scale transport or rotation. Other regions with fast and thick lithosphere situated in the presence of significant continental deformation, such as the Tarim Basin (e.g., Molnar & Tapponnier, 1981), the Sichuan Basin (e.g., Klemperer et al., 2006), and the Ordos Block in Asia, appear to impede crustal flow and not participate in the surrounding deformational processes except near their margins. Thus, the thick lithosphere of Arctic-Alaska challenges rotational transport models and may be more consistent with fixist models of the evolution of the region. Alternately, the high mantle velocities could result from lithosphere that subducted during the formation of the Brooks Range and foundered afterwards. Attempting to resolve this dichotomy is beyond the scope of this paper.

Close inspection of **Figures 14a** and **14b** reveals that the high velocity anomalies beneath Arctic-Alaska extend under the Brooks Range and move southward with increasing depth. This can be seen more clearly in vertical profile E-E' shown in **Figure 21**, where it appears that the upper mantle underlying the region underthrusts the Brooks Range. The geometry of the thick lithosphere relative to the location of the Brooks Range provides additional information for tectonic reconstructions of the region. Jiang et al. (2018) also image high velocities in the mantle beneath Arctic-Alaska, which appear to extend further southward at greater depths.

7. Conclusions

We present a radially anisotropic 3-D model of Vsv and Vsh for the crust and uppermost mantle to a depth of 120 km beneath Alaska and surroundings using Rayleigh wave group and phase speed and Love wave phase speed measurements. We acquire waveforms from all broad-band seismic stations across the study region openly available from January 2001 to February 2019, totaling more than 500 stations taken from 22 networks (Transportable Array, Alaska Networks, etc.), to perform both ambient noise and earthquake tomography. Rayleigh wave phase speed maps extend from 8 to 85 s period whereas the group speed maps and the Love wave phase speed maps range from 8 to 50 s. These data and corresponding uncertainties are the basis for the inversion for the 3-D model across the study region.

The 3-D model derives from a Bayesian Monte Carlo procedure applied on a grid spacing of approximately 50 km. The prior distribution spans broad bounds around the reference model, in which the sedimentary characteristics and Moho depth come from CRUST-1.0 and crustal and mantle wave speeds come from 1-D model ak135. Constraints limit the accepted models to be vertically smooth between interfaces and relatively simple, which is a hypothesis that is tested in the inversion. The inversion results in a posterior distribution of models beneath each grid point, which we summarize at each point and depth with the mean ($\bar{m}$), which we refer to as the "mean model", and standard deviation (σ_m), which we refer to as "uncertainty". Shen and Ritzwoller (2016) argue that σ_m is not an ideal estimate of absolute model uncertainty, as it overestimates nonsystematic error and does not explicitly quantify systematic error, but it does provide information about relative uncertainty. We find that we can constrain the shear wave structures relatively well in the middle of the crust and mantle. but internal interfaces are not determined as accurately.

For the vast majority of the region of study, the average model fits the dispersion data well with misfit χ (eqn. (3)) smaller than 2.0 for our final mean model. The data cannot be fit without introducing apparent radial anisotropy, but a very simple parameterization in which mantle and crustal radial anisotropy are spatially variable but respectively constant with depth at each point suffices to fit the data. Crustal anisotropy is represented either with a depth-constant value in the crystalline crust (γ_c) or sediments (γ_c) depending on sedimentary thickness. Typically, $\gamma_s \gg \gamma_c > \gamma_m$, with values of γ_s (determined only in the Colville Basin) being greater than 20%, and values of γ_c and γ_m running up to 8% depending on location. With the current data set we are not justified in inferring a model that possesses more vertical variability of apparent radial anisotropy.

Many structural features are determined reliably in the final 3-D model, and we mention a few in this paper. (1) Apparent crustal radial anisotropy is strongest across a broad swath of central and northern Alaska, coincident with areas identified by Miller & Hudson (1991) that were subjected to significant Cretaceous extensional deformation. (2) Apparent radial anisotropy in the sediments of the Colville basin is very strong, presumably caused by sedimentary stratification and layering. (3) Crustal thickness estimates are similar to those based on receiver functions by Miller & Moresi (2018). (4) The uppermost mantle beneath Arctic-Alaska is a high velocity feature that extends at least to 120 km depth, which may be more consistent with fixist models for the evolution of the region than more popular rotational transport models. (5) The slab geometry of the Alaskan subduction zone that we image is largely consistent with the Alaska_3D 1.0 model of Jadamec & Billen (2010), with the principal exception being what we call the Yakutat “slab shoulder region”. Our model also confirms the existence of structural features that have been reported by recent studies, including what we call the “Barren Islands slab anomaly” which is a relative low velocity anomaly in the upper mantle that was also observed by Yang & Gao (2019), the “Alaskan aseismic slab edge” that was also observed by Jiang et al. (2018) and Gou et al. (2019), the “Wrangellia slab anomaly” that was also imaged by Gou et al. (2019), and subducting Yakutat lithosphere seaward of the Wrangell volcanic field (Martin-Short et al., 2018; Jiang et al., 2018; Gou et al., 2019). The “Yakutat slab shoulder region” is a high-speed anomaly in our model in the upper mantle, which has not been reported in previous studies.

The 3-D model presented here should be a useful reference for a variety of purposes, including for earthquake location and predicting other types of geophysical data. However, future work is needed to continue to improve both the Vsv and Vsh parts of the model. For example, observations of the Rayleigh wave H/V ratio would help to improve the shallowest parts of the model and receiver functions may be added to help refine internal interfaces. However, receiver functions in Alaska are often complicated and strongly spatially variable, similar in many respects to those in Tibet even though the Tibetan crust is much thicker. The multi-station common Moho conversion point (CMCP) stacking method (e.g. Deng et al., 2015) may yield better information than single-station based stacking or harmonic stripping methods such as those applied across the lower 48 states by Shen and Ritzwoller (2016), for example. There are many other fertile directions to pursue in order to improve and extend the model, but we mention only one more. Once Rayleigh wave azimuthal anisotropy is estimated, those measurements can be added to the data presented here to invert for an integrated model of inherent anisotropy represented by the depth-dependent tilted elastic tensor, as described by Xie et al., (2015, 2017).

Acknowledgments

This research was supported by NSF grant EAR-1928395 at the University of Colorado at Boulder. The facilities of IRIS Data Services, and specifically the IRIS Data Management Center, were used for access to waveforms, related metadata and/or derived products used in this study. IRIS Data Services are funded through the Seismological Facilities for the Advancement of Geoscience and EarthScope (SAGE) Proposal of the National Science Foundation under Cooperative Agreement EAR-1261681. This work utilized the RMACC Summit supercomputer, which is supported by the National Science Foundation (awards ACI-1532235 and ACI-1532236), the University of Colorado Boulder, and Colorado State University. The Summit supercomputer is a joint effort of the University of Colorado Boulder and Colorado State University.

References

Allam, A.A., V. Schulte-Pelkum, Y. Ben-Zion, C. Tape, N. Ruppert, and Z.E. Ross, Ten kilometer vertical Moho offset and shallow velocity contrast along the Denali fault zone from double-difference tomography, receiver functions, and fault zone head waves, Tectonophysics, 721, 56-69, 2017.

Amante, C. and Eakins, B.W., ETOPO1 arc-minute global relief model: procedures, data sources and analysis, 2009.

Babuska, V., Seismic Anisotropy in the Earth, Modern Approaches in Geophysics, Vol. 10, Kluwer Academic Publishers, 1991.

Barmin, M.P., M.H. Ritzwoller, and A.L. Levshin, A fast and reliable method for surface wave tomography, Pure Appl. Geophys., 158(8), 1351 - 1375, 2001.

Bensen, G.D., M.H. Ritzwoller, M.P. Barmin, A.L. Levshin, F. Lin, M.P. Moschetti, N.M. Shapiro, and Y. Yang, Processing seismic ambient noise data to obtain reliable broad-band surface wave dispersion measurements, Geophys. J. Int., 169, 1239-1260, doi: 10.1111/j.1365-246X.2007.03374.x, 2007.

Bird, K.J. and C.M. Molenaar, The North Slope Foreland Basin, Alaska, in Foreland Basins and Fold Belts, eds. R.W. Macqueen and D.A. Leckie, Ch. 13, 363-393, 1992.

Brocher, T. M., Empirical relations between elastic wave speeds and density in the Earth's crust, Bull. Seismol. Soc. Am., 95, 2081–2092, doi:10.1785/0120050077, 2005.

Christensen, D.H. and G.A. Abers, Seismic anisotropy under central Alaska from SKS splitting observations, J. Geophys. Res., 115, B04315, 2010.

Coney, P.J. and D.L. Jones, Accretion tectonics and crustal structure of Alaska, Tectonophys., 119, 265-283, 1985.

Deng, Y., W. Shen, T. Xu, and M.H. Ritzwoller, Crustal layering in northeastern Tibet: A case study based on joint inversion of receiver functions and surface wave dispersion, Geophys. J. Int., 203(1), 692-706, doi:10.1093/gji/ggv321, 2015.

Eberhart-Phillips, D.H. Christensen, T.M. Brocher, R. Hansen, N.A. Ruppert, P.J. Haeussler, and G.A. Abers, Imaging the transition from Aleutian subduction to Yakutat collision in central Alaska, with local earthquakes and active source data, J. Geophys. Res., 111, B11303, 2006.

Ekstrom, G. and A.M. Dziewonski, The unique anisotropy of the Pacific upper mantle, Nature, 394, 168-172, 1998.

Erdman, M.E., Hacker, B.R., Zandt, G. & Seward, G., Seismic anisotropy of the crust: electron-backscatter diffraction measurements from the Basin and Range, Geophys. J. Int., **195**(2), 1211–1229, 2013.

Feng, L. and M.H.Ritzwoller, The effect of sedimentary basins on surface waves that pass through them, Geophys. J. Int., 211(1), 572-592, doi:10.1093/gji/ggx313, 2017.

Ferris, A., G.A. Abers, D.H. Christensen, and E. Veenstra, High resolution image of the subducted Pacific (?) plate beneath central Alaska, 50-150 km depth, Earth Planet. Sci. Letts., 214, 575-588, 2003.

Freymueller, J.T., H. Woodard, S.C. Cohen, R. Cross, J. Elliott, C.F. Larsen, S. Hreinsdottir, and C. Zweck, Active deformation processes in Alaska, based on 15 years of GPS measurements, Active Tectonics and Seismic Potential of Alaska, Geophys. Monogr. Ser. 179, 1-42, 2008.

Fuis, G.S., A.R. Levander, W.J. Lutter, E.S. Wissinger, T.E. Moore, and N.I. Christensen, Seismic images of the Brooks Range, Arctic Alaska, reveal crustal-scale duplexing, Geology, 23(1), 65-68, 1995.

Fuis, G.S., T.E. Moore. G. Plafker, T.M. Brocher, M.A. Fisher, W.D. Mooney, W.J. Nokleberg, R.A. Page, B.C. Beaudoin, N.I. Christensen, A.R. Levander, W.J. Lutter, R.W. Saltus, N.A. Ruppert, Trans-Alaska crustal transect and continental evolution involving subduction underplating and synchronous foreland thrusting, Geology, 36(3), 267-270, 2008.

Gou T., D. Zhao, Z. Huang, and L. Wang, Aseismic deep slab and mantle flow beneath Alaska: Insight from anisotropic tomography. Journal of Geophysical Research: Solid Earth, in press, 2019.

Hacker, B. R., and G.A. Abers, Subduction Factory 3: An Excel worksheet and macro for calculating the densities, seismic wave speeds, and H2O contents of minerals and rocks at pressure and temperature, Geochem., Geophys., Geosyst., 5, Q01005, doi:10.1029/2003GC000614., 2004.

Hacker, B.R., M.H. Ritzwoller, and J. Xie, Central Tibet has a partially melted, mica-bearing crust, Tectonics, 33, doi:10.1002/2014TC003534, 2014.

Hanna, J., and M.D. Long, SKS splitting beneath Alaska: Regional variability and implications for subduction processes at a slab edge, Tectonophysics, 530-531, 272-285, 2012.

Hayes, G.P. and D.J. Wald, Slab1.0: A three-dimensional model of global subduction zone geometries, J. Geophys. Res: Solid Earth, 117(B1), 2012.

Haynie, K.L. and M.A. Jadamec, Tectonic drivers of the Wrangell block: Insights on fore-arc sliver processes from 3-d geodynamic models of Alaska, Tectonics, 36, 1180-1206, 2017.

Herrmann, R. B. (2013) Computer programs in seismology: An evolving tool for instruction and research, Seism. Res. Lettr. **84**, 1081-1088, doi:10.1785/0220110096

Jadamec, M.A. and M.I. Billen, Reconciling surface plate motions with rapid three-dimensional mantle flow around a slab edge, Nature, 465 (7296), 338, 2010.

Jiang, C., Schmandt, B., Ward, K. M., Lin, F.-C., & Worthington, L. L., Upper mantle seismic structure of Alaska from Rayleigh and S wave tomography, Geophysical Research Letters, 45, 10,350–10,359, 2018.

Johnston, S.T., The Great Alaskan Terrane Wreck: reconciliation of paleomagnetic and geological data in the northern Cordillera, Earth Planet. Sci. Letts., 193 259-272, 2001.

Kennett, B.L.N., Engdahl, E.R. & Buland, R., Constraints on seismic velocities in the Earth from travel times, Geophys J. Int., **122,** 108–124, 1995.

Klemperer, S.L., 2006. Crustal flow in Tibet: a review of geophysical evidence for the physical state of Tibetan lithosphere. In: Searle, M.P., Law, R.D. (Eds.), Channel Flow, Ductile Extrusion and Exhumation of Lower Mid-crust in Continental Collision Zones: Geol. Soc. Spec. Publ., 268, pp. 39–70, 2006.

Kustowski, B., G. Ekström, and A. M. Dziewoński (2008), Anisotropic shear-wave velocity structure of the Earth's mantle: A global model, J. Geophys. Res. Solid Earth, 113(B6), B06306, doi:10.1029/2007JB005169.

Laske, G., Masters., G., Ma, Z. and Pasyanos, M., Update on CRUST1.0 - A 1-degree Global Model of Earth's Crust, Geophys. Res. Abstracts, 15, Abstract EGU2013-2658, 2013.

Levandowski, W., C. Jones, W. Shen, M.H. Ritzwoller and V. Schulte-Pelkum, Origins of topography in the Western US: Mapping crustal and upper mantle density variations using a uniform seismic velocity model, J. Geophys. Res., 119, 2375-2396, doi: 10.1002/2013JB010607, 2014.

Lin, F.-C. and M.H. Ritzwoller, Helmholtz surface wave tomography for isotropic and azimuthally anisotropic structure, Geophys. J. Int., 17 pages, doi: 10.1111/j.1365-246X.2011.05070.x, 2011.

Lin, F.-C., M.P. Moschetti, and M.H. Ritzwoller, Surface wave tomography of the western United States from ambient seismic noise: Rayleigh and Love wave phase velocity maps, Geophys. J. Int., doi:10.1111/j1365-246X.2008.03720.x, 2008.

Lin, F.-C., M.H. Ritzwoller, and R.K. Snieder, Eikonal tomography: Surface wave tomography by phase-front tracking across a regional broad-band seismic array, Geophys. J. Int., 177(3), 1091-1110, 2009.

Marone, F., Y. Gung, and B. Romanowicz, Three-dimensional radial anisotropic structure of the North American upper mantle from inversion of surface waveform data, Geophys. J. Int., 171(1), 206-222, 2007.

Martin-Short, R., R. M. Allen, and I. D. Bastow, Subduction geometry beneath south central Alaska and its relationship to volcanism, Geophys. Res. Lett., 43, 9509–9517, 2016.

Martin-Short, R., R. Allen, I.D. Bastow, R.W. Poritt, and M.S Miller, Seismic imaging of the Alaska subduction zone: Implications for slab geometry and volcanism, Geochem., Geophys., Geosys., 19, 4551-4560, 2018.

Miller, E.L. and T.L. Hudson, Mid-Cretaceous extensional fragmentation of the Jurassic-Early Cretaceous compressional orogeny, Alaska, Tectonics, 10(4), 781-796, 1991.

Miller, M.S. and L. Moresi, Mapping the Alaskan Moho, Seis. Res. Lett., 89(6), 2439-2436, 2018.

Miller, M.S., L. O'Driscoll, R.W. Poritt, and S.M. Roeske, Multiscale crustal architecture of Alaska inferred from P receiver functions, Lithosphere, 10(2), 267-278, 2018.

Molnar, P. & Tapponnier, P. A., possible dependence of tectonic strength on the age of the crust in Asia. Earth Planet. Sci. Lett. 52, 107–114, 1981.

Montagner, J.P., and T. Tanimoto, Global upper mantle tomography of seismic velocities and anisotropies, J. Geophys. Res., 96, 20,337- 20,351, 1991

Moore, T.E. and S.E. Box, Age, distribution, and style of deformation in Alaska north of 60 N: Implications for assembly of Alaska, Tectonophys., 691, 133-170, 2016.

Moschetti, M.P., M.H. Ritzwoller, and F.C. Lin, Seismic evidence for widespread crustal deformation caused by extension in the western USA, Nature, 464, Number 7290, 885-889, 8 April 2010.

Mosegaard, K., and A. Tarantola, Monte Carlo sampling of solutions to inverse problems, J. Geophys. Res., 100(B7), 12,431–12,447, doi:10.1029/94JB03097, 1995.

Nettles, M., and A. M. Dziewoński, Radially anisotropic shear velocity structure of the upper mantle globally and beneath North America, J. Geophys. Res., 113, 27 pp., doi:200810.1029/2006JB004819, 2008.

O'Driscoll, L.J. and M.S. Miller, Lithospheric discontinuity structure in Alaska, thickness variations determined by Sp receiver functions, Tectonics, 34, 694-714, 2015.

Perttu A, D. Christensen, G. Abers G, X. Song, Insights into mantle structure and flow beneath Alaska based on a decade of observations of shear wave splitting, Journal of Geophysical Research: Solid Earth, 119(11):8366-77, 2014.

Ritzwoller, M.H. and L. Feng, Overview of pre- and post-processing of ambient noise correlations, In N. Nakata, L. Gualtieri, and A. Fichtner (Eds.), Ambient Seismic Noise (pp. 144-187), Cambridge, Cambridge University Press, doi:10.1017/9781108264808.007, 2019.

Ritzwoller, M.H., F.C. Lin, and W. Shen, Ambient noise tomography with a large seismic array, Compte Rendus Geoscience, 13 pages, doi:10.1016/j.crte.2011.03.007, 2011.

Rondenay, S., L.G.J. Montesi, and G.A. Abers, New geophysical insight into the origin of the Denali volcanic gap, Geophys. J. Int., 182, 613-630, 2010.

Shapiro, N.M. and M.H. Ritzwoller, Monte-Carlo inversion for a global shear velocity model of the crust and upper mantle, Geophys. J. Int., 151, 88-105, 2002.

Shapiro, N.M., M.H. Ritzwoller, P. Molnar, and V. Levin, Thinning and flow of Tibetan crust constrained by seismic anisotropy, Science, 305, 233-236, 9 July 2004.

Shen, W. and M.H. Ritzwoller, Crustal and uppermost mantle structure beneath the United States, J. Geophys. Res. Solid Earth, doi:10.1002/2016JB012887, 2016.

Shen, W., M.H. Ritzwoller, V. Schulte-Pelkum, F.-C. Lin, Joint inversion of surface wave dispersion and receiver functions: A Bayesian Monte-Carlo approach, Geophys. J. Int., 192, 807-836, doi:10.1093/gji/ggs050, 2013.

Thomsen, L., Weak elastic anisotropy, Geophysics, **51**(10), 1954– 1966, 1986.

Tian, Y. and D. Zhao, Seismic anisotropy and heterogeneity in the Alaska subduction zone, Geophys. J. Int., 190, 629-649, 2012.

Wang, Y. and C. Tape, Seismic velocity structure and anisotropy of the Alaska subduction zone based on surface wave data, J. Geophys. Res., 119, 8845-8865, 2014.

Ward, K. M., Ambient noise tomography across the southern Alaskan Cordillera, Geophys. Res. Lett., 42, 3218–3227, 2015.

Ward, K.M. and F.-C. Lin, Lithospheric structure across the Alaska Cordillera from the joint inversion of surface waves and receiver functions, J. Geophys. Res., 123, 8780-8797, 2018.

Wiemer, S., G. Tytgat, M. Wyss, and U. Duenkel, Evidence for shear-wave anisotropy in the mantle wedge beneath South Central Alaska, Bull. Seism. Soc. Am, 89(5), 1313-1322, 1999.

Xie, J., M. H. Ritzwoller, W. Shen, Y. Yang, Y. Zheng, and L. Zhou, Crustal radial anisotropy across Eastern Tibet and the Western Yangtze Craton, J. Geophys. Res. Solid Earth, 118(8), 4226–4252, doi:10.1002/jgrb.50296, 2013.

Xie, J., M.H. Ritzwoller, S. Brownlee, and B. Hacker, Inferring the oriented elastic tensor from surface wave observations: Preliminary application across the Western US, Geophys. J. Int., 201, 996-1021, 2015.

Xie, J., M.H. Ritzwoller, W. Shen, and W. Wang, Crustal anisotropy across Eastern Tibet and surroundings modeled as a depth-dependent tilted hexagonally symmetric medium, Geophys. J. Int., 209, 466-491, doi: 10.1093/gji/ggx004, 2017.

Yang, X., and H. Gao, Seismic imaging of slab segmentation and correlation with volcano distribution along the Aleutian-Alaska subduction zone, Nature Communications, submitted, 2019.

Yang, X. and K.M. Fischer, Seismic anisotropy beneath the Shumagin Islands segment of the Aleutian-Alaska subduction zone, J. Geophys. Res., 100(B9), 18,165018,177, 1995.

Yuan, H.Y., Romanowicz, B., Fischer, K.M. & Abt, D., 2011. 3-D shear wave radially and azimuthally anisotropic velocity model of the North American upper mantle, Geophysical Journal International, 184**,** 1237-1260.

Zhang, Y., A. Li, and H. Hu, Crustal structure in Alaska from receiver function analysis, Geophysical Research Letters, 46, 2019.

Zhao, D., D. Christensen, and H. Pulpan, Tomographic imaging of the Alaska subduction zone, J. Geophys. Res., 100B4), 6487-6504, 1995.

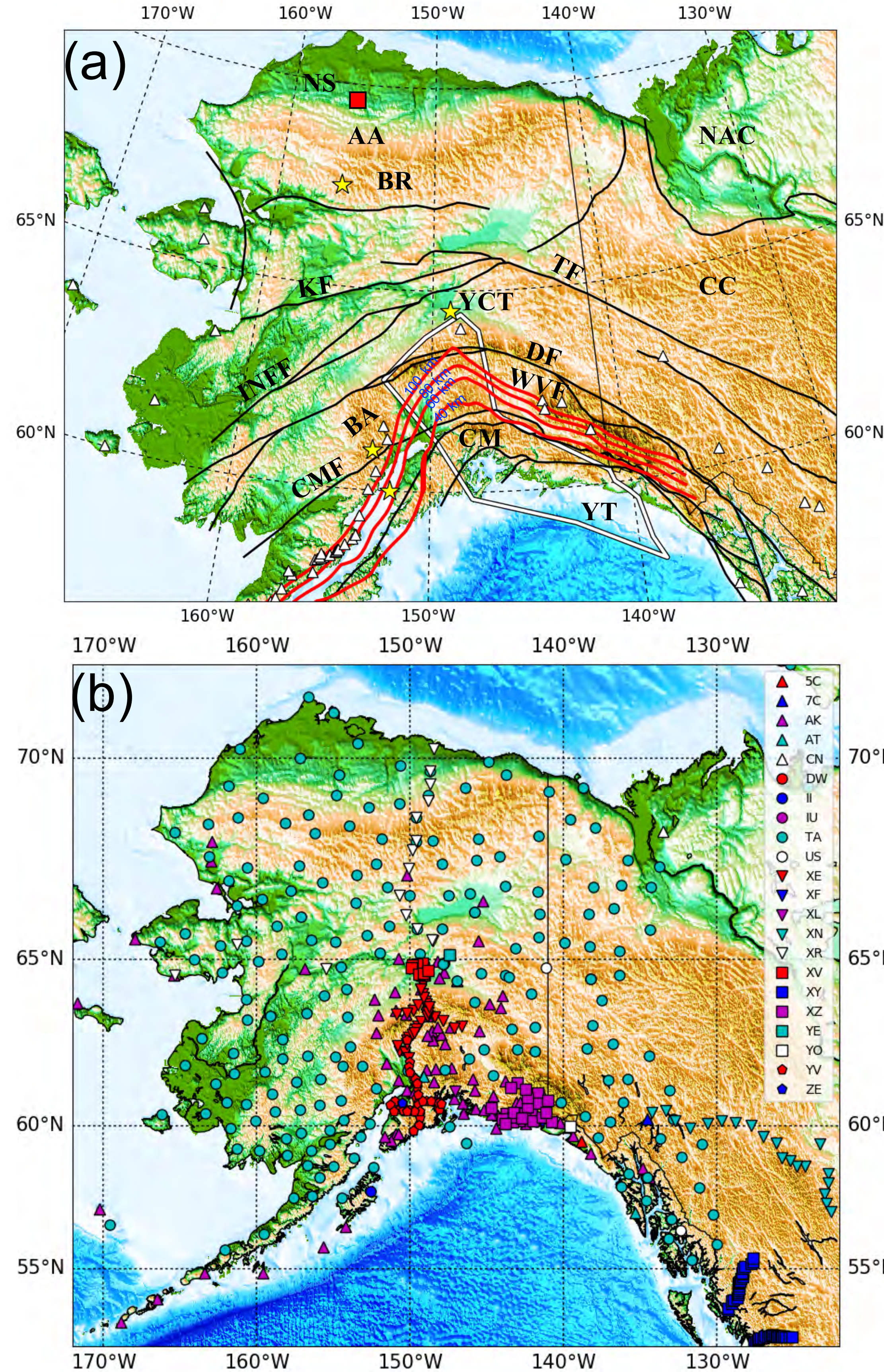
(a)
170°W
160°W
150°W
140°W
130°W
65°N
60°N
NS
AA
BR
NAC
KF
TF
CC
YCT
INFF
DF
WVF
BA
CM
CMF
YT
100 km
80 km
60 km
40 km
(b)
70°N
65°N
60°N
55°N
5C
7C
AK
AT
CN
DW
II
IU
TA
US
XE
XF
XL
XN
XR
XV
XY
XZ
YE
YO
YV
ZE

972

Figure 1. (a) Geologic and tectonic features and nomenclature. The black curves are major faults, and the four red curves are top edges of the subducting Alaskan-Aleutian slab at different depths: from south to north: 40 km, 60 km, 80 km and 100 km (Jadamec and Billen, 2010). The white polygon is the hypothesized Yakutat Terrane (Eberhart-Phillips et al., 2006). Structural and tectonic features are identified with abbreviations explained in **Table 1**. The four yellow stars indicate sample grid points located in the Brooks Range (BR), the Aleutian slab Back-Arc region, the Cook Inlet, and the Yukon Composite Terrane (YCT) used in **Figures 2, 6, 7, 8, 10,** and **16**, and the red square is the location in the Colville Basin used in **Figure 7**. (b) Station distribution. There are 22 networks indicated with different symbols. The USArray Transportable Array and the Alaska Network are the largest networks, identified with green circles and purple triangles, respectively.

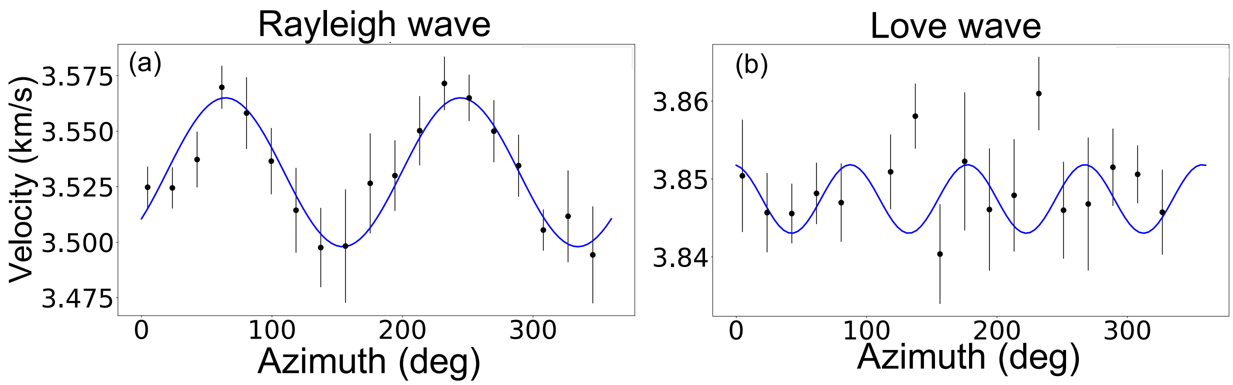

Figure 2. Azimuthal bin-averaged phase velocity measurements and bin standard deviations plotted versus azimuth (θ) measured using the eikonal tomography method in the Yukon Composite Terrane at 20 s period. (a) For Rayleigh waves, we fit a 2θ curve to the bin averages, where θ is azimuth. (b) For Love waves, we fit a 4θ curve. Interpretation of the azimuthal variation of the measurements is beyond the scope of this paper.

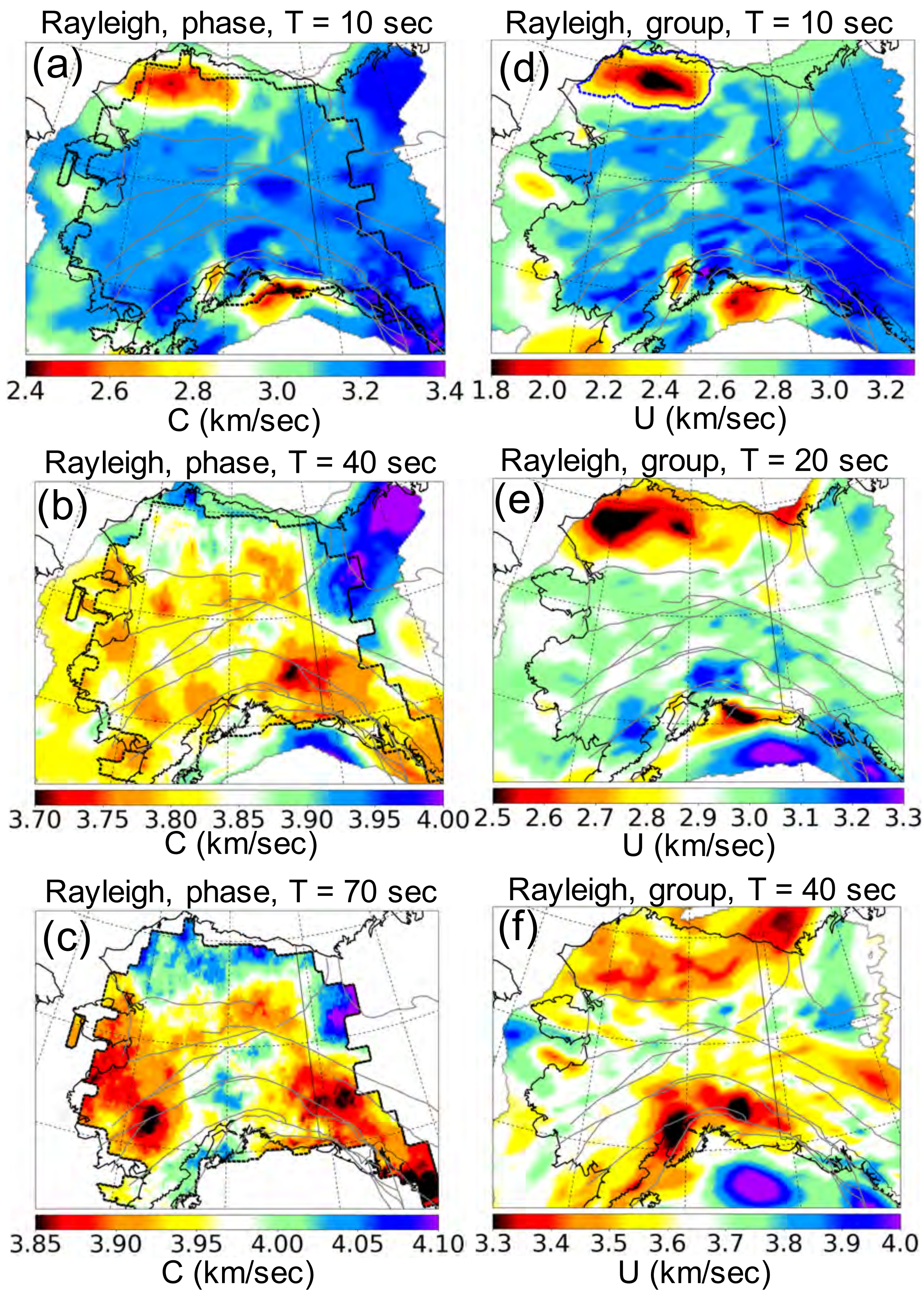

Figure 3. (a) - (c) Rayleigh wave phase speed maps at periods of 10 s, 40 s, and 70 s. The 10 s map is constructed from ambient noise tomography (ANT), 40 s is from a combination of

ambient noise and earthquake tomography (ET), and the 70 s map is from ET alone. (d) - (f) Rayleigh wave group speed maps for periods of 10 s, 20 s, and 40 s constructed with ANT. The black piece-wise linear contours in the left column enclose the regions where eikonal tomography is performed. Outside of these contours and for the maps in the right column ray theoretic tomography is performed (Barmin et al., 2001). The dark blue dotted contour in (d) indicates the location of the North Slope Foreland Basin (Colville Basin), where the 10 s Rayleigh wave group speed is less than 2.5 km/s.

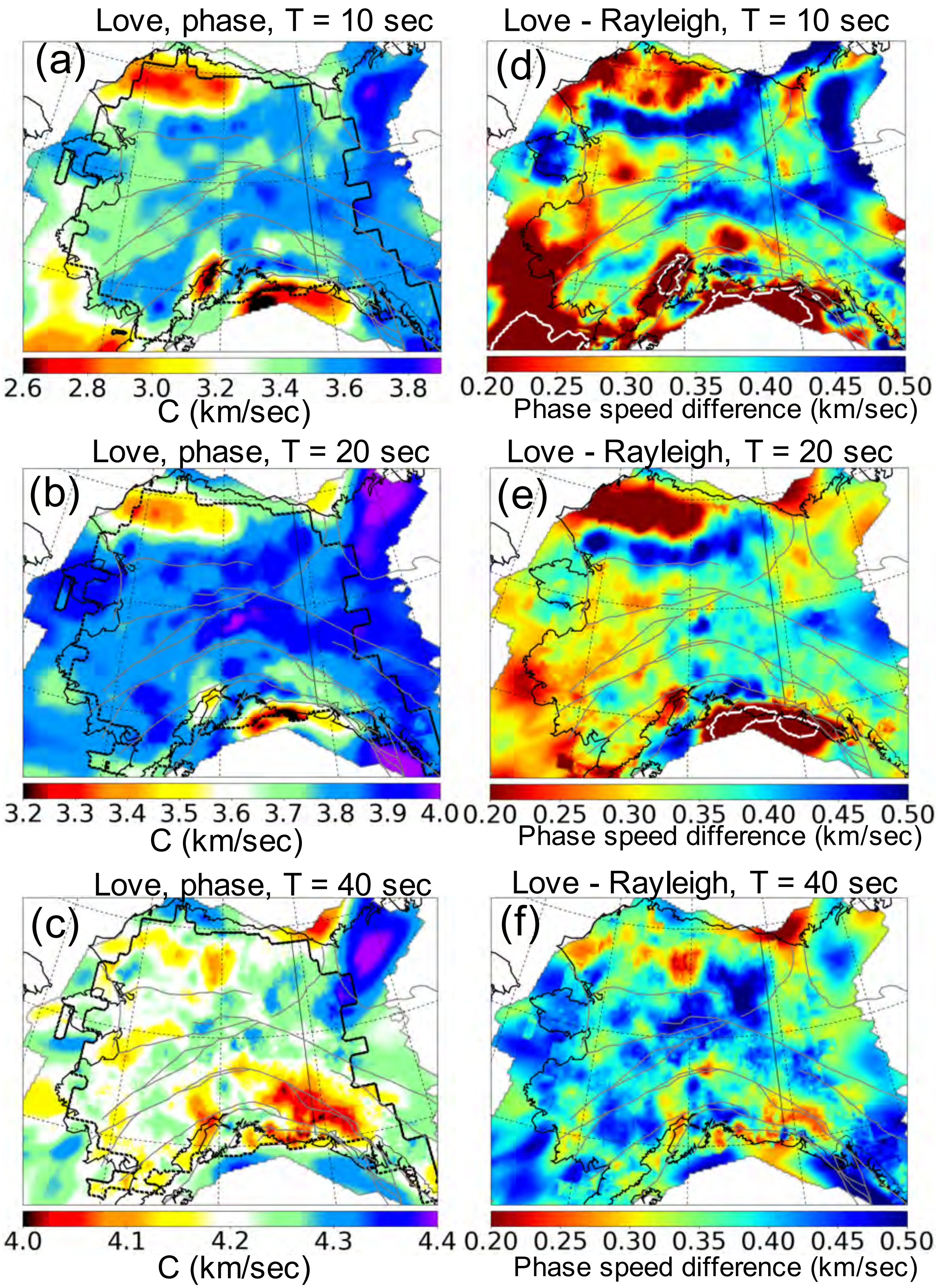
Love, phase, T = 10 sec
(a)
2.6 2.8 3.0 3.2 3.4 3.6 3.8
C (km/sec)
Love - Rayleigh, T = 10 sec
(d)
0.20 0.25 0.30 0.35 0.40 0.45 0.50
Phase speed difference (km/sec)
Love, phase, T = 20 sec
(b)
3.2 3.3 3.4 3.5 3.6 3.7 3.8 3.9 4.0
C (km/sec)
Love - Rayleigh, T = 20 sec
(e)
0.20 0.25 0.30 0.35 0.40 0.45 0.50
Phase speed difference (km/sec)
Love, phase, T = 40 sec
(c)
4.0 4.1 4.2 4.3 4.4
C (km/sec)
Love - Rayleigh, T = 40 sec
(f)
0.20 0.25 0.30 0.35 0.40 0.45 0.50
Phase speed difference (km/sec)

1003

Figure 4. (a) - (c) Love wave phase speed maps at periods of 10 s, 20 s, and 40 s, where the 10 s and 20 s maps are constructed using ambient noise tomography (ANT), and 40 s is from a combination of ANT and earthquake tomography. (d) - (f) Differences in phase speed between Love waves and Rayleigh waves at 10 s, 20 s, and 40 s, respectively. The black piece-wise linear contours in the left column enclose the regions where eikonal tomography is performed. Outside of these contours ray theoretic tomography is performed (Barmin et al., 2001). The white contours in (d) and (e) are regions where the Love wave is slower than the Rayleigh wave, which occurs in wet regions.

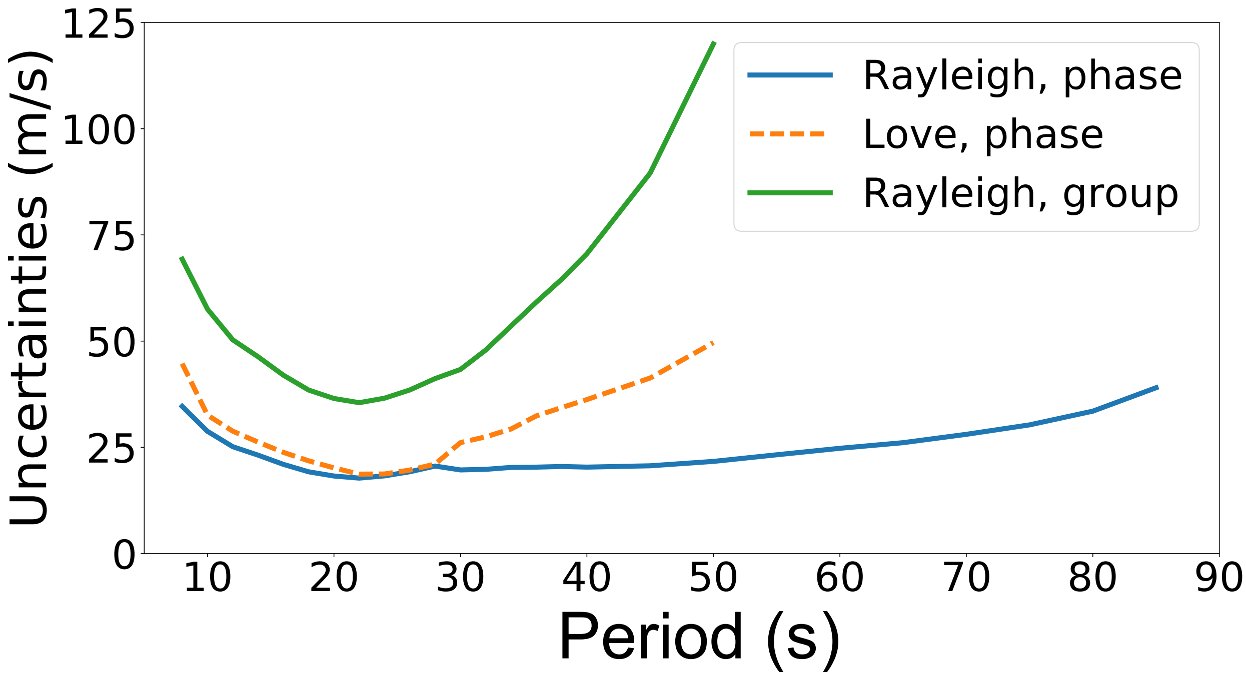

Figure 5. Estimated measurement uncertainties as a function of period averaged across the study region. The legend identifies the wave type for each curve. These uncertainties are twice the standard deviation of the mean of azimuthally binned standard deviations that result from eikonal tomography (e.g., **Fig. 2**).

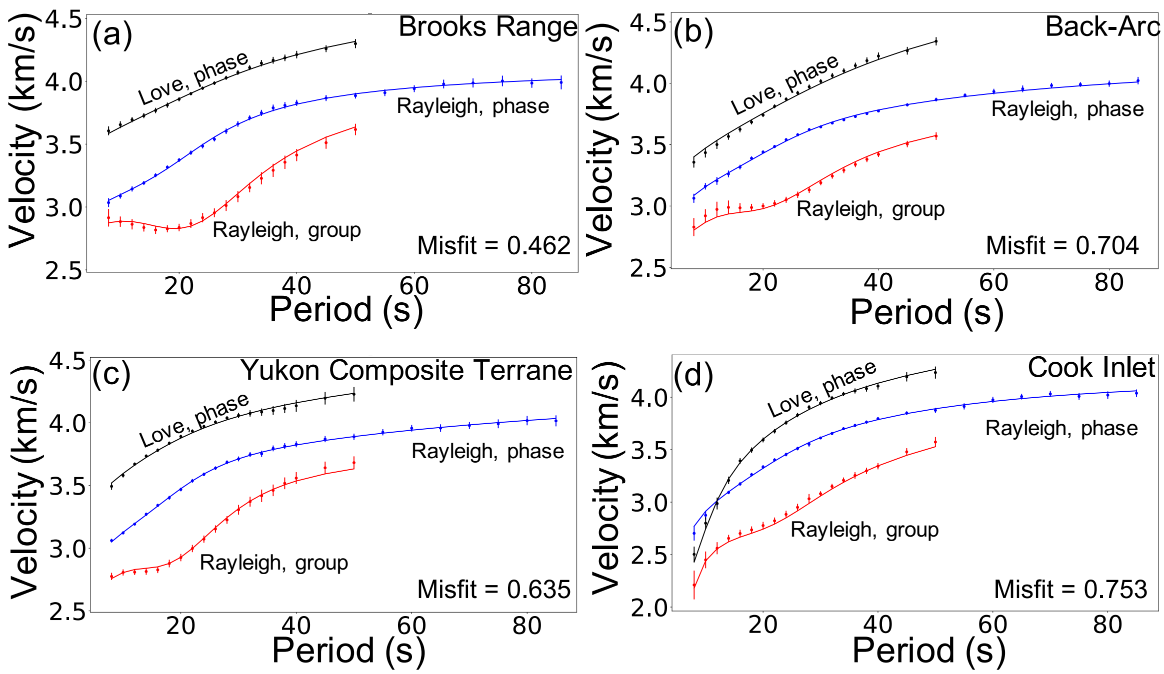

Figure 6. Examples of the Rayleigh wave phase and group speed curves and Love wave phase speed curves at four locations identified with yellow stars in **Fig. 1**: (a) Brooks Range, (b) Aleutian Back-Arc, (c) Yukon Composite Terrane, and (d) Cook Inlet. The error bars (blue: Rayleigh wave phase, red: Rayleigh wave group, black: Love wave phase) are observed dispersion measurements with one standard deviation uncertainties. Solid curves (blue: Rayleigh wave phase, red: Rayleigh wave group, black: Love wave phase) are predictions from the 3-D model, namely the mean of the posterior distribution of models at each depth including crustal and mantle anisotropy (Vsv, Vsh). Misfit is defined by equation (3).

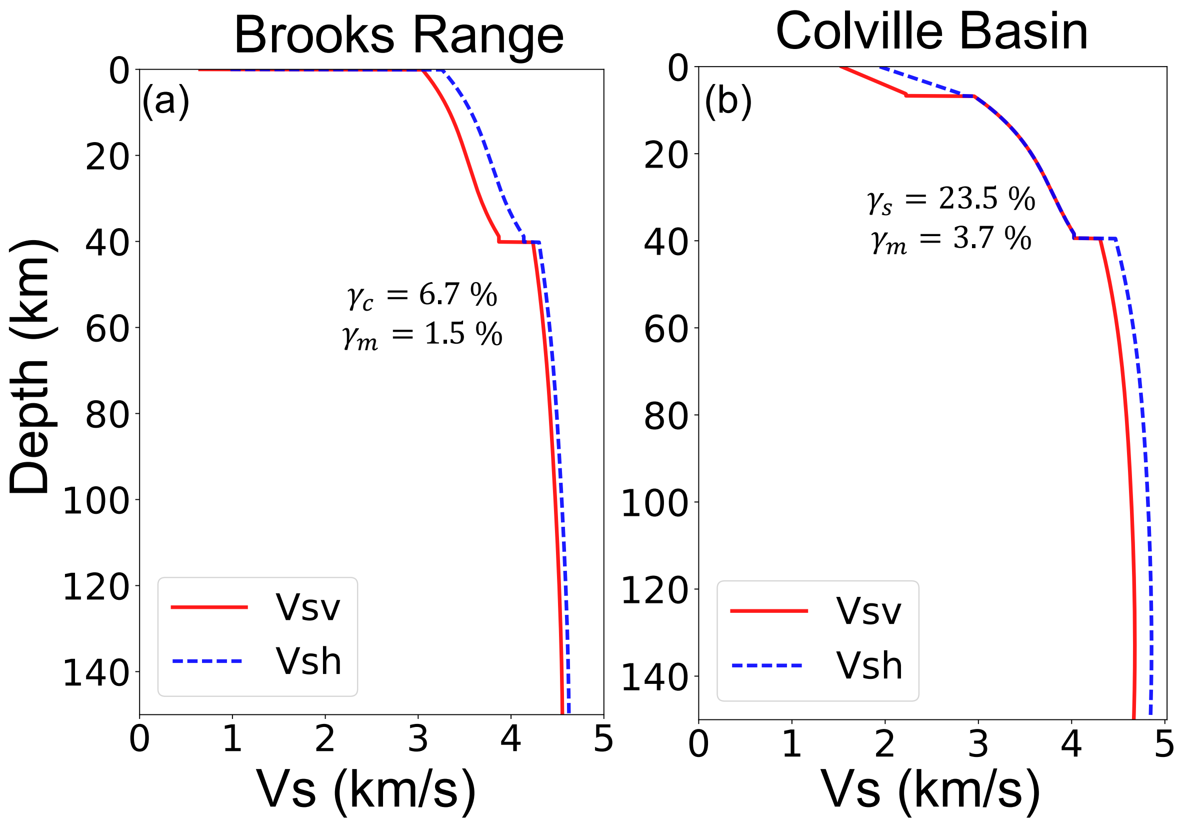

Figure 7. Examples of the mean of the posterior distribution plotted versus depth. (a) Brooks Range (yellow star in **Fig. 1a**), Vsv and Vsh profiles with crustal and mantle anisotropy but no sedimentary anisotropy ($\gamma_s = 0, \gamma_c \neq 0 \neq \gamma_m$). (b) Colville Basin (red square in **Fig. 1a**), Vsv and Vsh profiles with sedimentary anisotropy and mantle anisotropy but no crustal anisotropy ($\gamma_c = 0, \gamma_s \neq 0 \neq \gamma_m$).

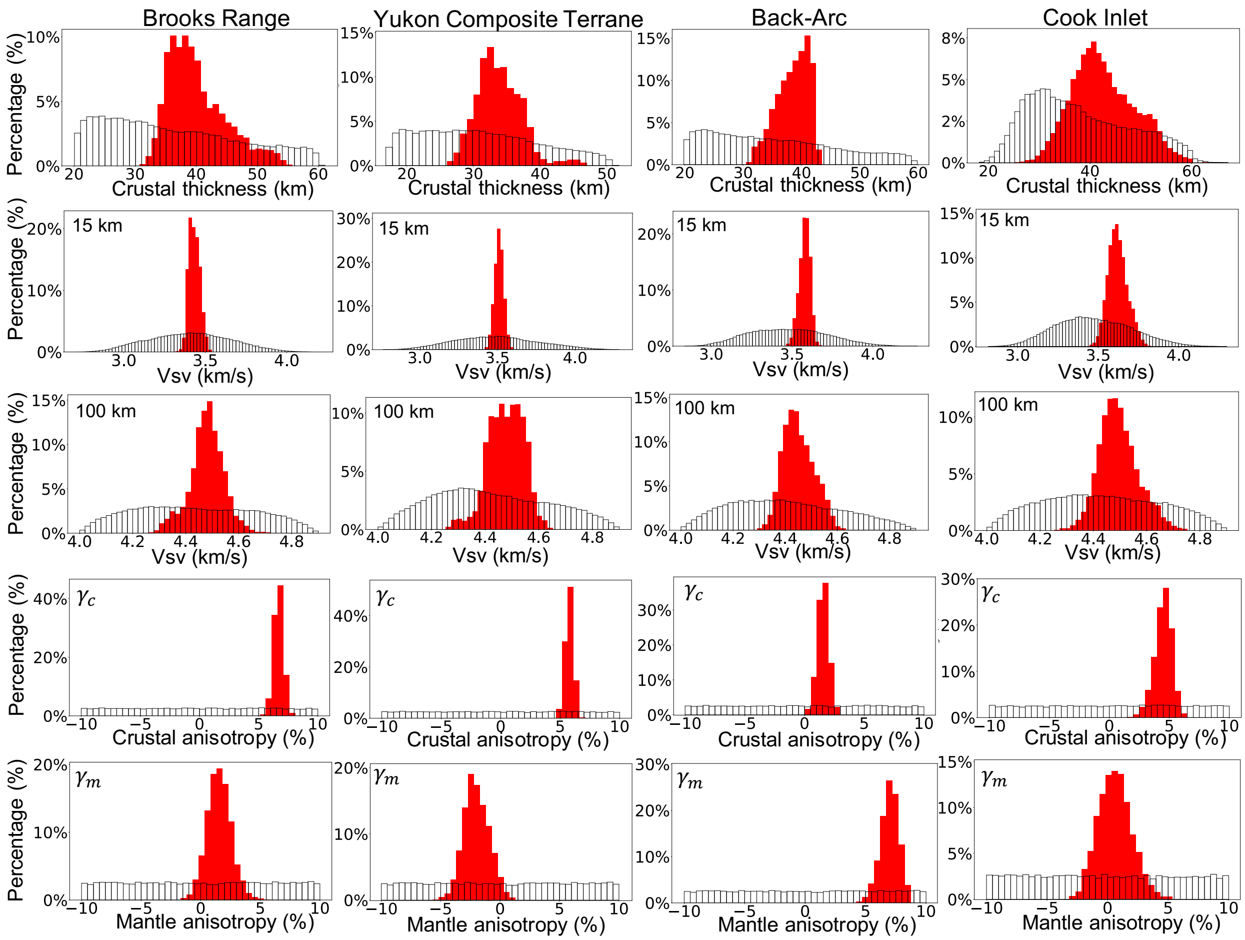

Figure 8. Examples of the prior and posterior marginal distributions for five model variables: crustal thickness, Vsv at depths of 15 km and 100 km, and crustal and mantle anisotropy (γ_c,γ_m) for the four locations identified with yellow stars in **Fig. 1** (Brooks Range, Yukon Composite Terrane, Aleutian Back-Arc, Cook Inlet). The prior distributions are shown with white histograms whereas the red histograms indicate the posterior distributions.

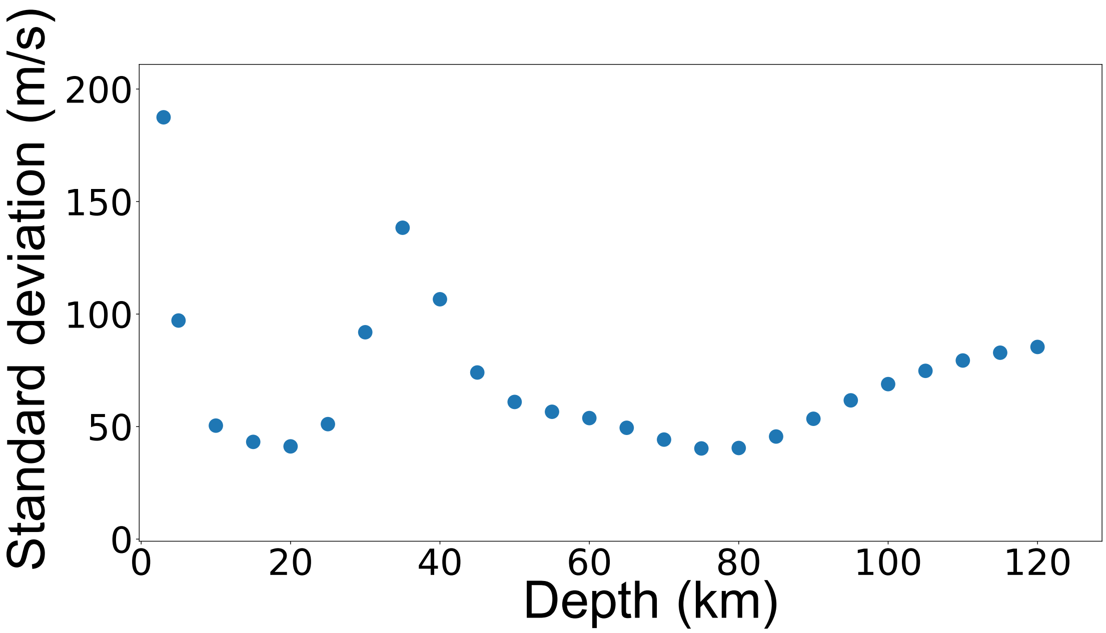

Figure 9. The standard deviation of the posterior distribution of Vsv presented as a function of depth averaged over the region of study.

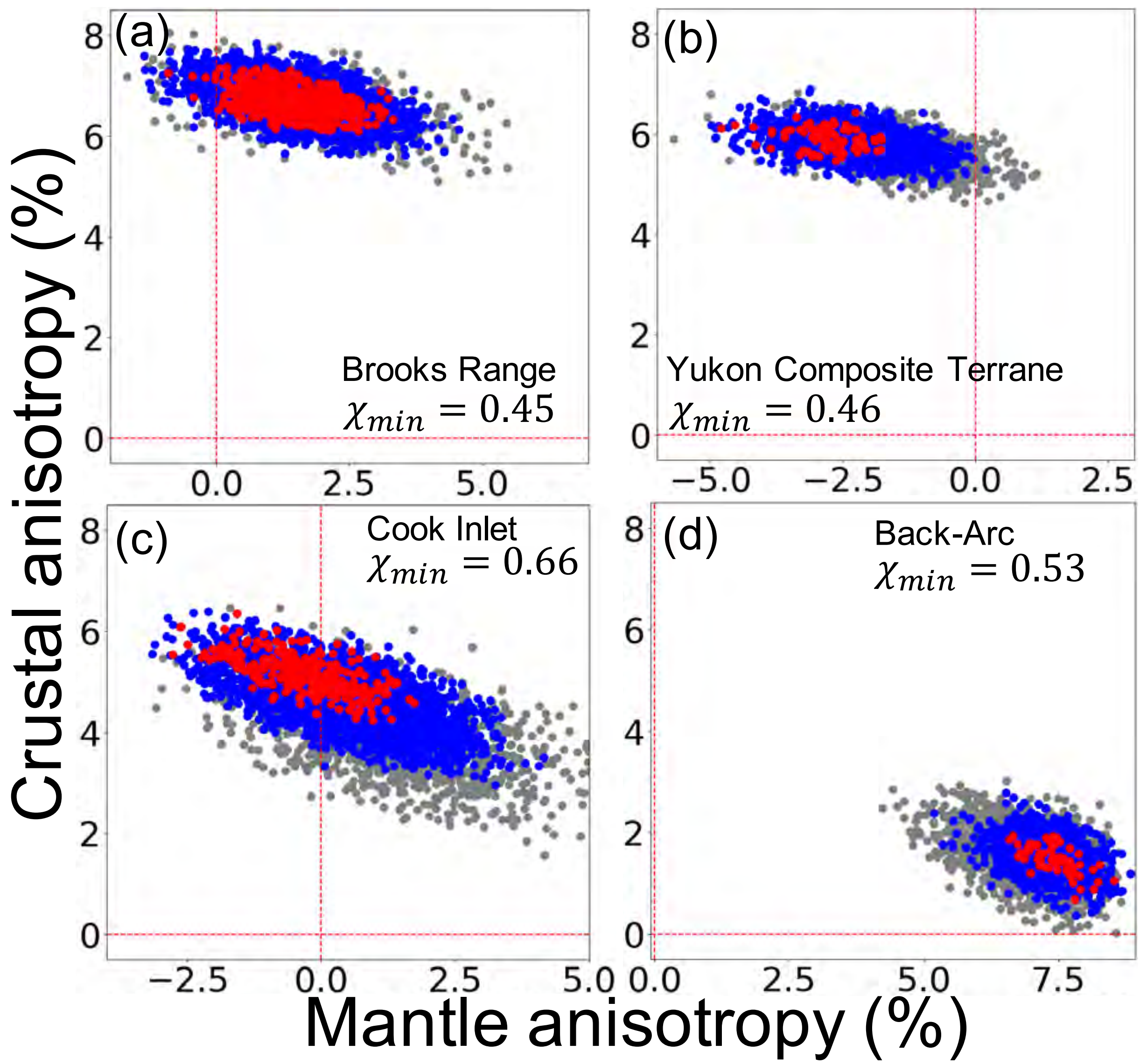

Figure 10. Trade-offs between crustal and mantle anisotropy (γ_c, γ_m) at the four locations identified with yellow stars in **Fig. 1**: (a) Brooks Range, (b) Yukon Composite Terrane, (c) Cook Inlet, and (d) Aleutian Back-Arc. Symbol color indicates misfit χ from each of the accepted models, defined by equation (3). Red: $\chi < \chi_{\min} + 0.2$, Blue: $\chi_{\min} + 0.2 \leq \chi < \chi_{\min} + 0.3$, Grey: $\chi_{\min} + 0.3 \leq \chi < \chi_{\min} + 0.5$, where $\chi_{\min}$ is the misfit from the best-fitting model at each location, which is labeled on each panel.

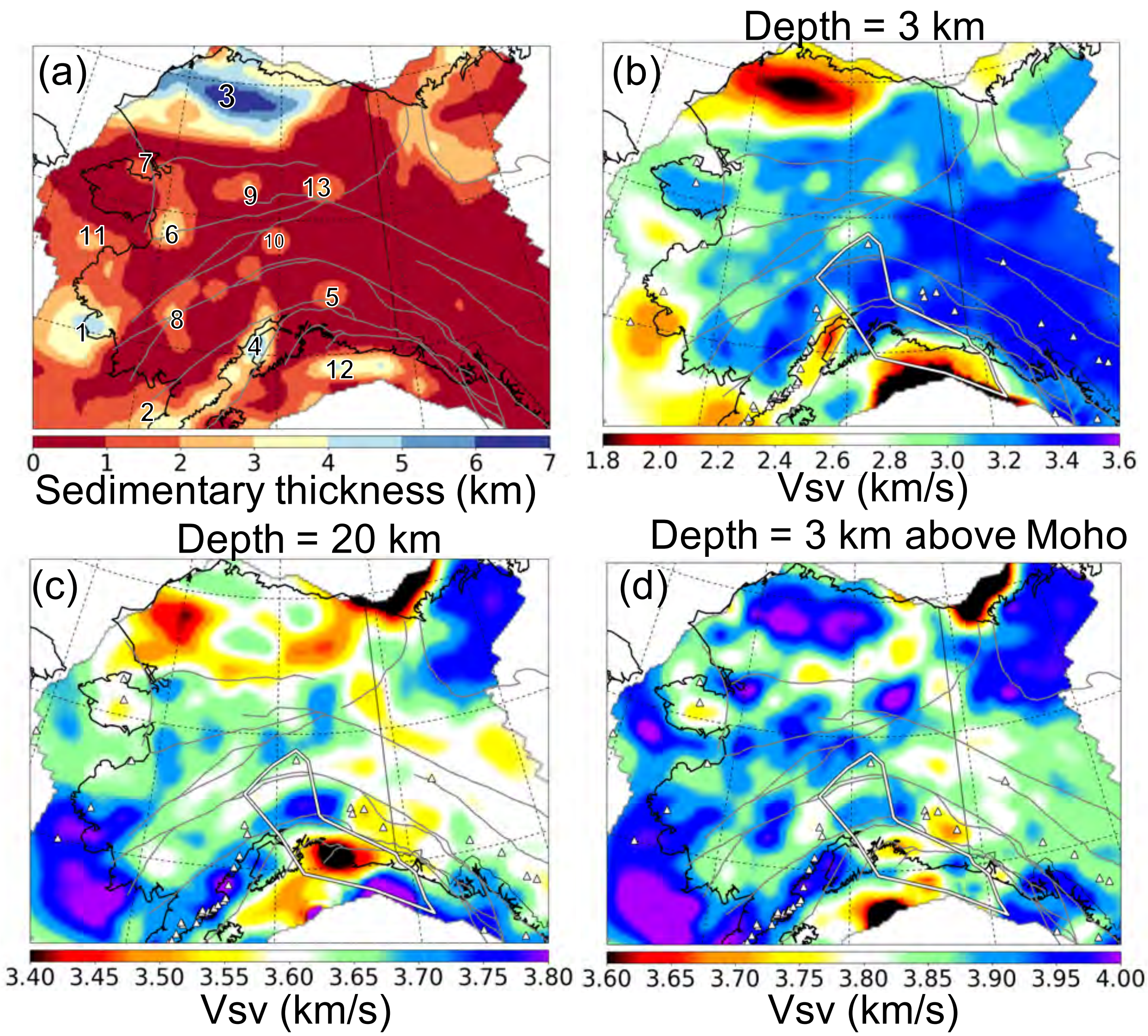

Figure 11. (a) Sedimentary thickness constructed with the mean of the posterior distribution of models, where the numbers and **Table 4** identify basin names. (b) – (d) The mean of the posterior distribution of Vsv for three depth ranges in the crust (central-depth ± 3 km) with central-depths of: (b) 3-km, (c) 20-km and (d) 3 km above Moho. Grey lines are major faults, the white polygon outlines the hypothesized Yakutat terrane, and triangles indicate volcanoes.

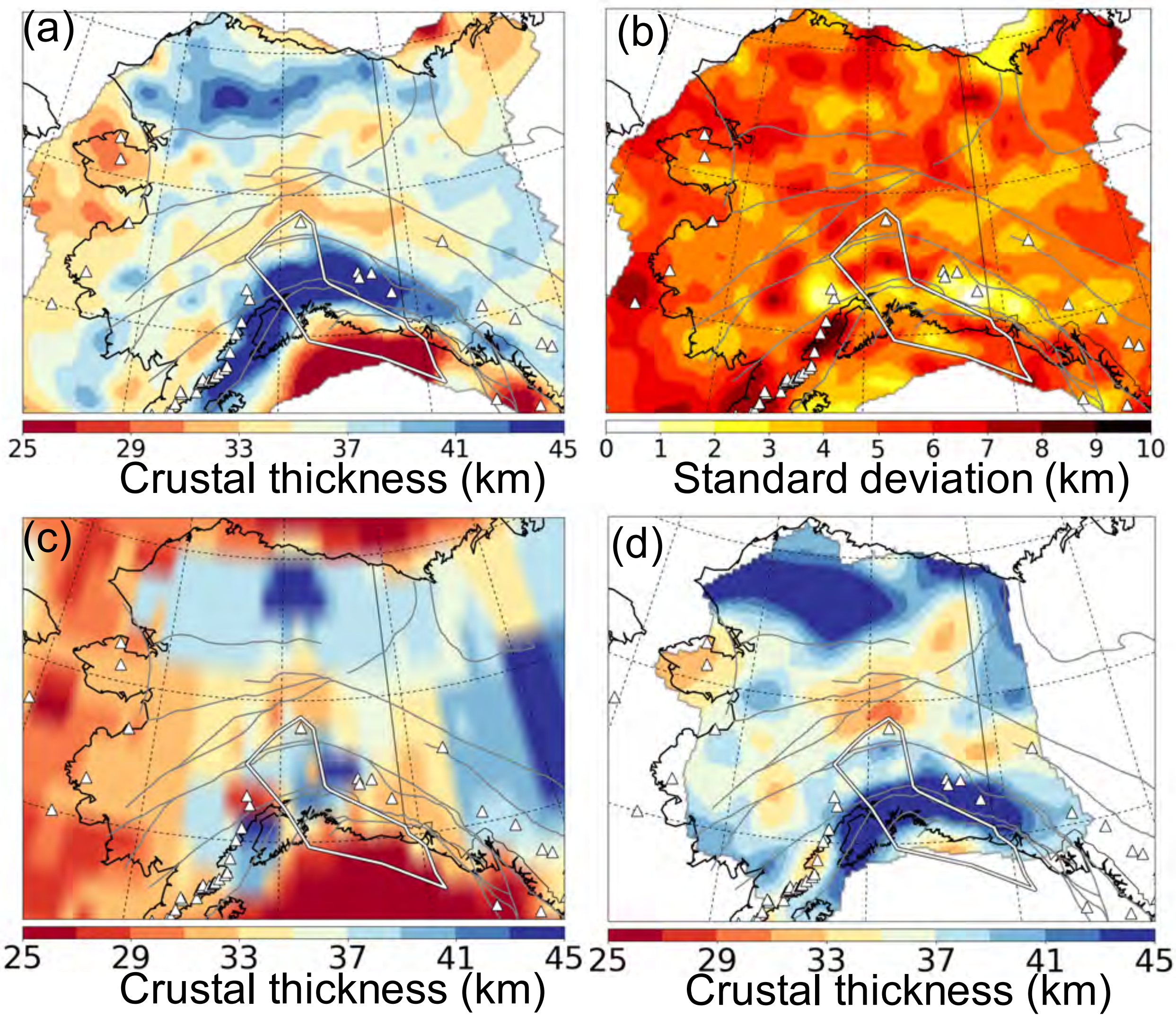

Figure 12. (a) Crustal thickness map constructed from the mean of the posterior distribution of models at each point. (b) Corresponding uncertainties of crustal thickness: standard deviation of the posterior distribution. (c) Crustal thickness from the Crust-1.0 model (Laske et al., 2013), which is part of the reference model used to define the prior distribution. (d) Crustal thickness estimated by Miller & Moresi (2018) using receiver functions, downloaded from https://github.com/lmoresi/miller-moho-binder .

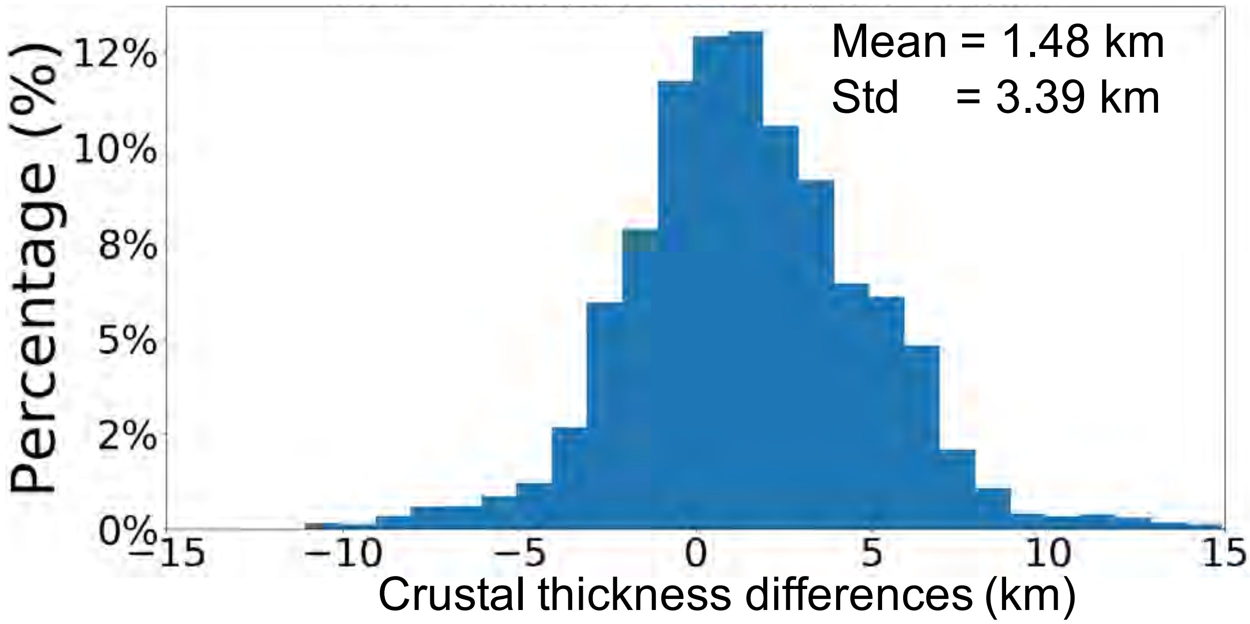

Figure 13. Histogram of differences in crustal thickness between our model and that of Miller & Moresi (2018), taken at grid-points where both models exist. The mean difference and standard deviation of the differences are listed.

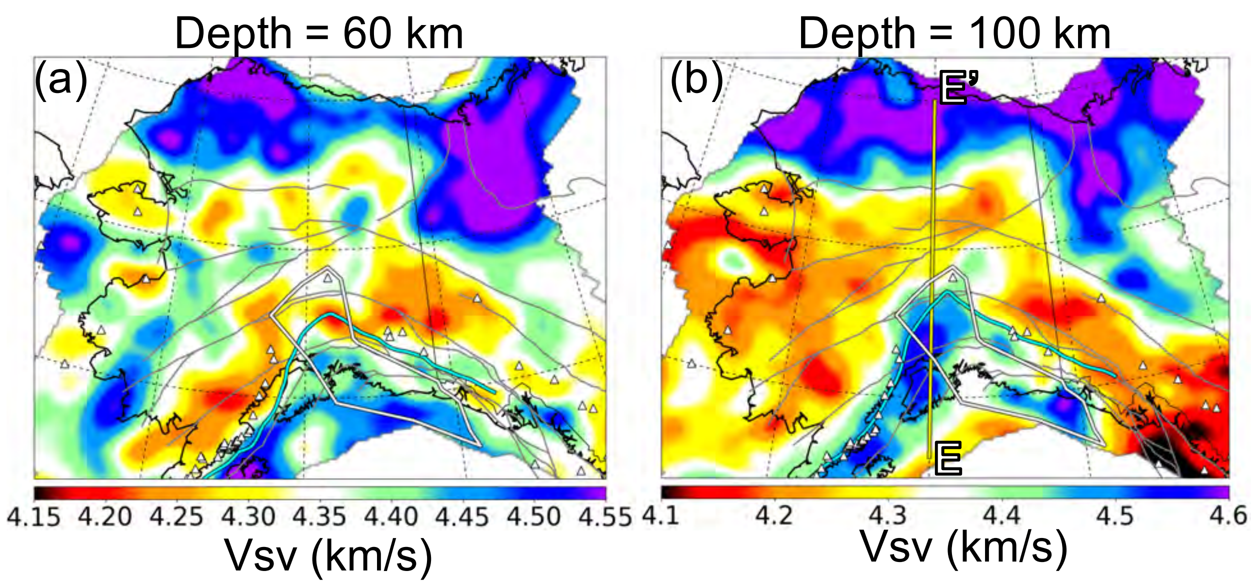

Figure 14. The mean of the posterior distribution of Vsv models at two depth ranges in the mantle (central-depth ± 3 km) with central-depths of: (a) 60-km and (b) 100-km. Symbols are similar to **Fig. 11**, but additionally the cyan curve is the top edge of the subducting slab at each map depth from the slab model of Jadamec & Billen (2010) and the lines E-E' identifies the vertical profile shown in **Fig. 21**.

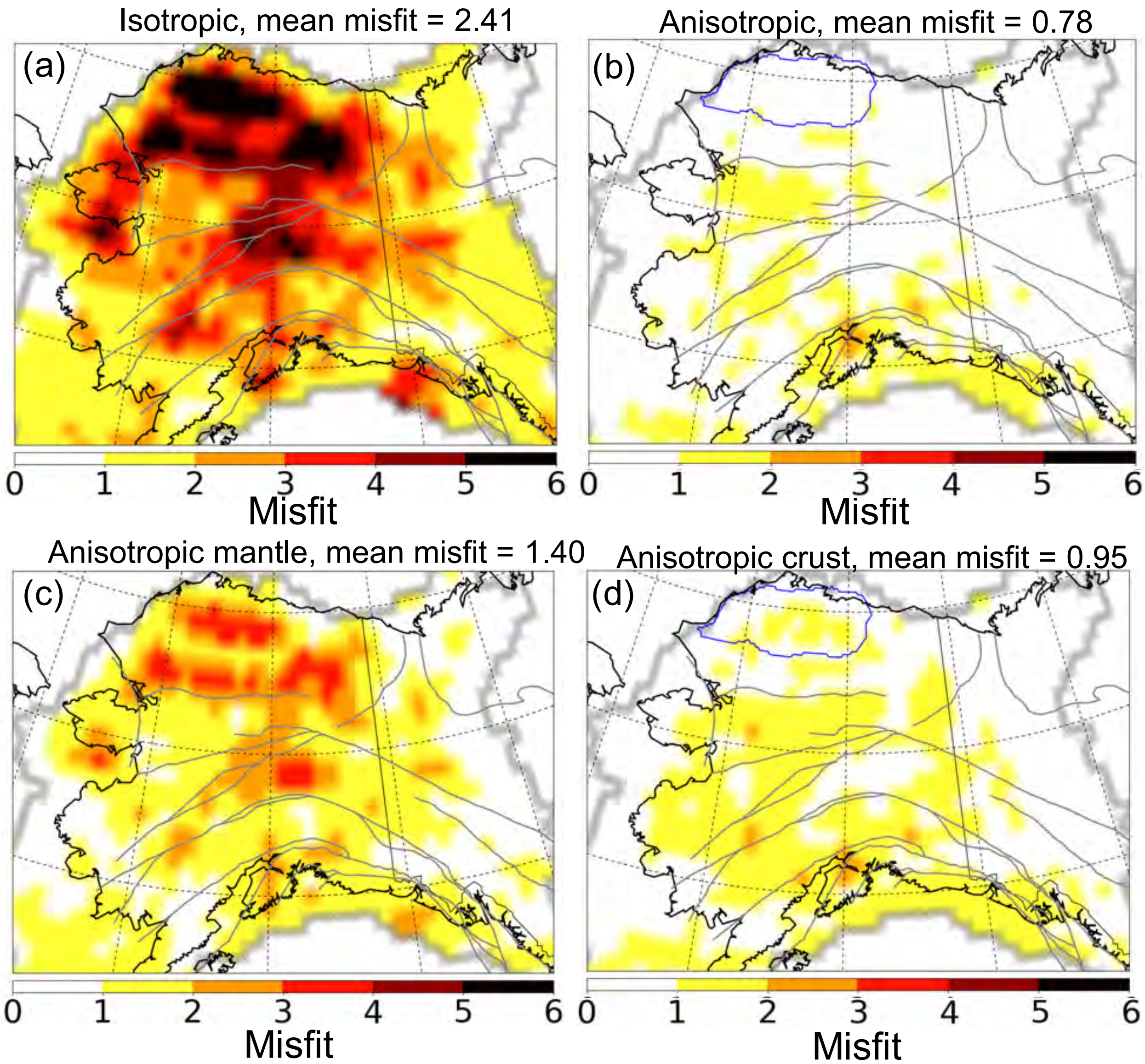

Figure 15. Misfit (defined by eqn. (3)) for the mean of posterior distribution of accepted models for different specifications of apparent radial anisotropy. (a) Isotropic model ($\gamma_s = \gamma_c = \gamma_m = 0$); inversion is performed using Rayleigh wave data alone. (b) Our final model based on both Rayleigh and Love wave data, including crustal and mantle anisotropy outside of the Colville Basin ($\gamma_s = 0, \gamma_c \neq 0 \neq \gamma_m$) and sedimentary and mantle anisotropy inside the Colville Basin ($\gamma_c = 0, \gamma_s \neq 0 \neq \gamma_m$). The Colville Basin is outlined in **Fig. 3d**. (c) The model is based on both Rayleigh and Love wave data and includes mantle anisotropy but no sedimentary or crustal anisotropy ($\gamma_s = 0 = \gamma_c, \gamma_m \neq 0$). (d) The model is based on both Rayleigh and Love wave data and includes crustal or sedimentary anisotropy but no mantle crustal anisotropy ($\gamma_m = 0, \gamma_c \neq 0$ or $\gamma_s \neq 0$). The mean of the misfit across each map is labeled at the top of each panel.

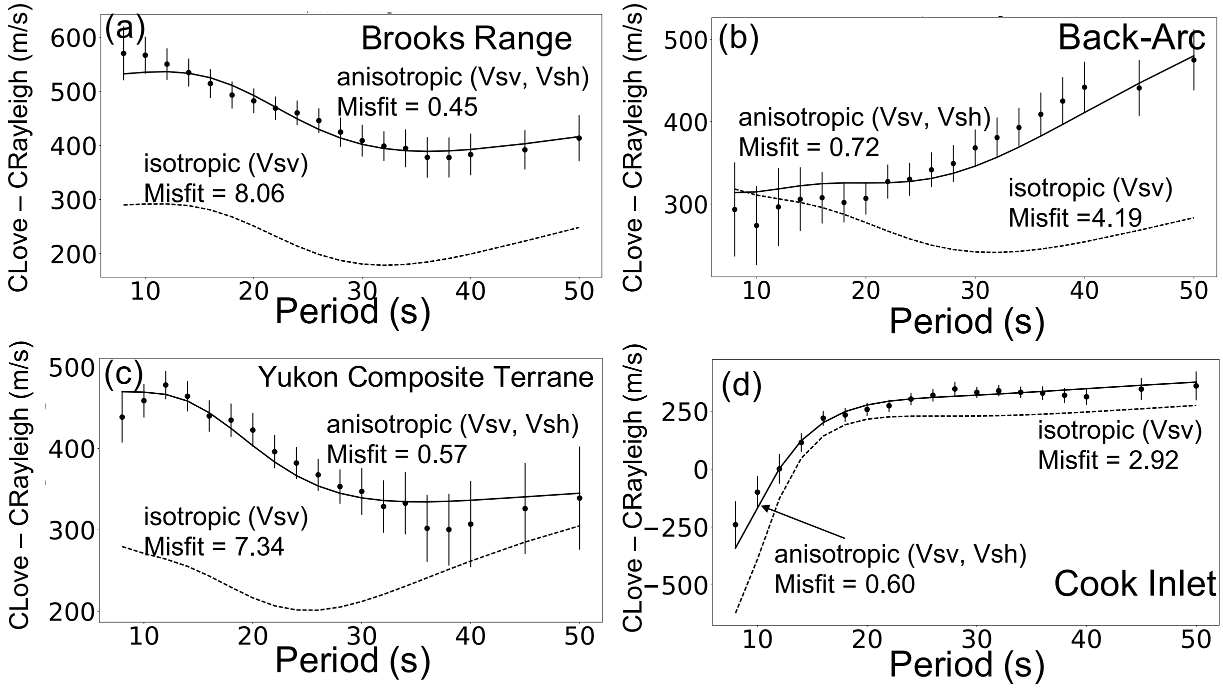

Figure 16. Examples of differences in phase speed between Love and Rayleigh waves at four locations identified with yellow stars in **Fig. 1**: (a) Brooks Range, (b) Aleutian Back-Arc, (c) Yukon Composite Terrane, and (d) Cook Inlet. The error bars are standard deviation uncertainties of the differences between Love and Rayleigh wave phase speeds. The solid lines are the predictions from the mean of the posterior distribution of our final radially anisotropic model ($\gamma_m \neq 0, \gamma_s \neq 0$ or $\gamma_c \neq 0$) and the black dashed lines are from the isotropic Vsv model ($\gamma_s = \gamma_c = \gamma_m = 0$). Misfit values from the isotropic and anisotropic models, defined by eqn. (3), are indicated on each panel.

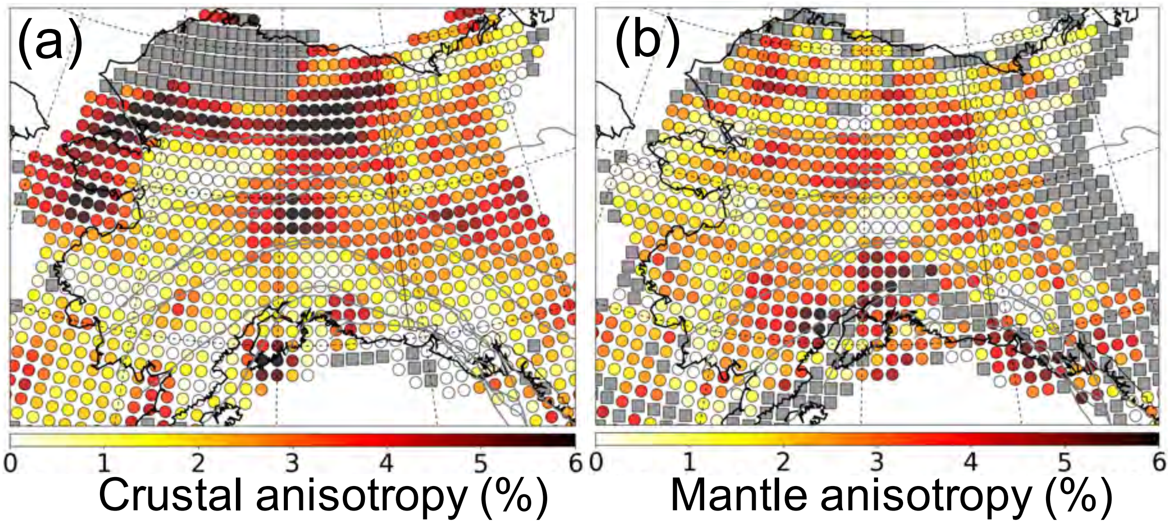

Figure 17. Apparent (a) crustal (γ_c) and (b) mantle (γ_m) radial anisotropy determined from the mean of the posterior distribution using both Rayleigh and Love wave data. The grey squares are grid nodes where we are not confident in the estimate of anisotropy. This includes the whole of the Colville Basin for crustal anisotropy.

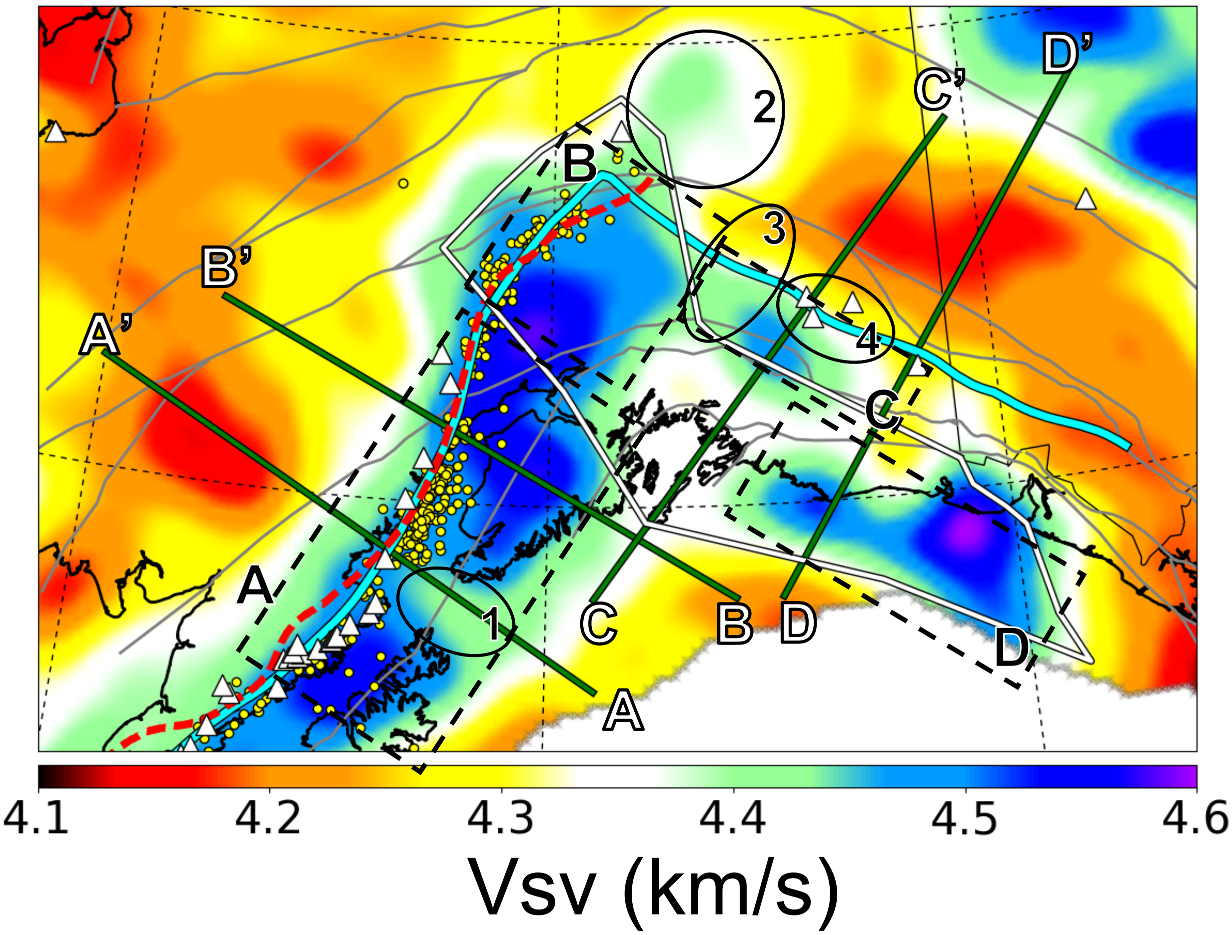

Figure 18. Blow up of the Vsv slice at 100 km with labels indicating different features of the subduction zone. Grey lines are major faults and the white contour outlines the hypothesized Yakutat Terrane. The cyan curve is the location of the edge of the subducting slab at 100 km depth from the slab model of Jadamec & Billen (2010) and the red dashed line delineates 100 km depth contour from the model Slab 1.0 (Hayes et al., 2012). The yellow dots indicate the locations of earthquakes from 1991 Jan to 2015 Oct (from ISC catalog) at depths from 95 – 105 km. Several tectonic features are identified with letters and numbers: A – Aleutian subduction zone; B – Alaskan subduction zone and slab kink which includes the Denali volcanic gap, C – Yakutat subduction zone, D – Yakutat slab shoulder. The numbered ovals indicate: 1 – the Barren Islands slab anomaly 2 – the aseismic slab edge, 3 – the Wrangellia slab anomaly and 4 – the Wrangell volcanic field. Vertical profiles A-A', B-B', C-C', and D-D' are shown in **Fig. 19**.

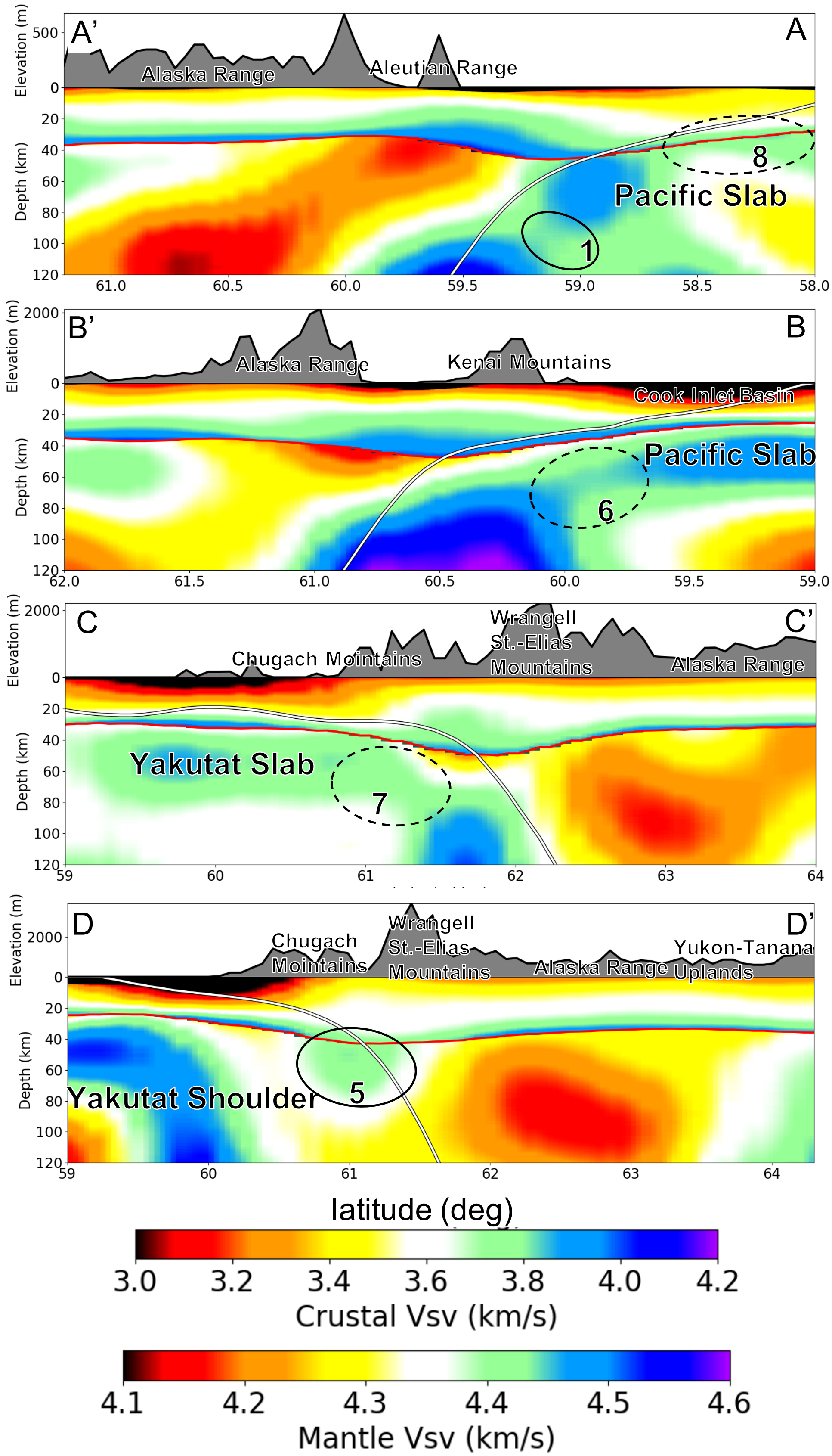
A'
A
Elevation (m)
Depth (km)
Alaska Range
Aleutian Range
8
Pacific Slab
1
B'
B
Alaska Range
Kenai Mountains
Cook Inlet Basin
Pacific Slab
6
C
C'
Wrangell St.-Elias Mountains
Chugach Moitains
Alaska Range
Yakutat Slab
7
D
D'
Chugach Moitains
Wrangell St.-Elias Mountains
Yukon-Tanana Uplands
Alaska Range
Yakutat Shoulder
5
latitude (deg)
Crustal Vsv (km/s)
Mantle Vsv (km/s)

1128

Figure 19. Vertical cross sections A-A’, B-B’, C-C’ and D-D’ identified in **Fig. 18**. The white lines in the cross-sections identify the upper edge of the subducting lithosphere in the model of Jadamec and Billen (2010). The black oval numbered 1 in profile A-A’ is the Barren Islands slab anomaly and other ovals are defined in the text. Dashed oval identify features we do not interpret and the solid ovals are features we do interpret.

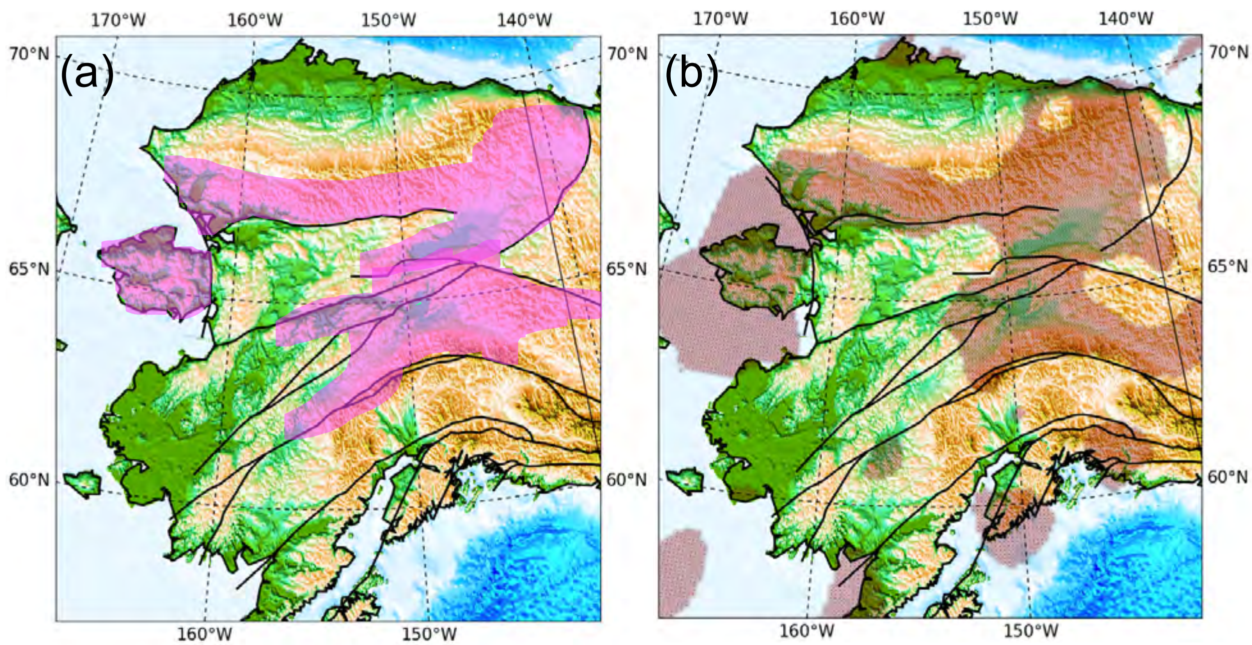

Figure 20. (a) Regions (colored in pink) identified by Miller & Hudson (1991) that have been subjected to significant mid-Cretaceous extension. (b) Regions (colored in brown) where we have confidence that the crustal anisotropy in the final model is considered to be stronger than average (γ_c >2.6 %).

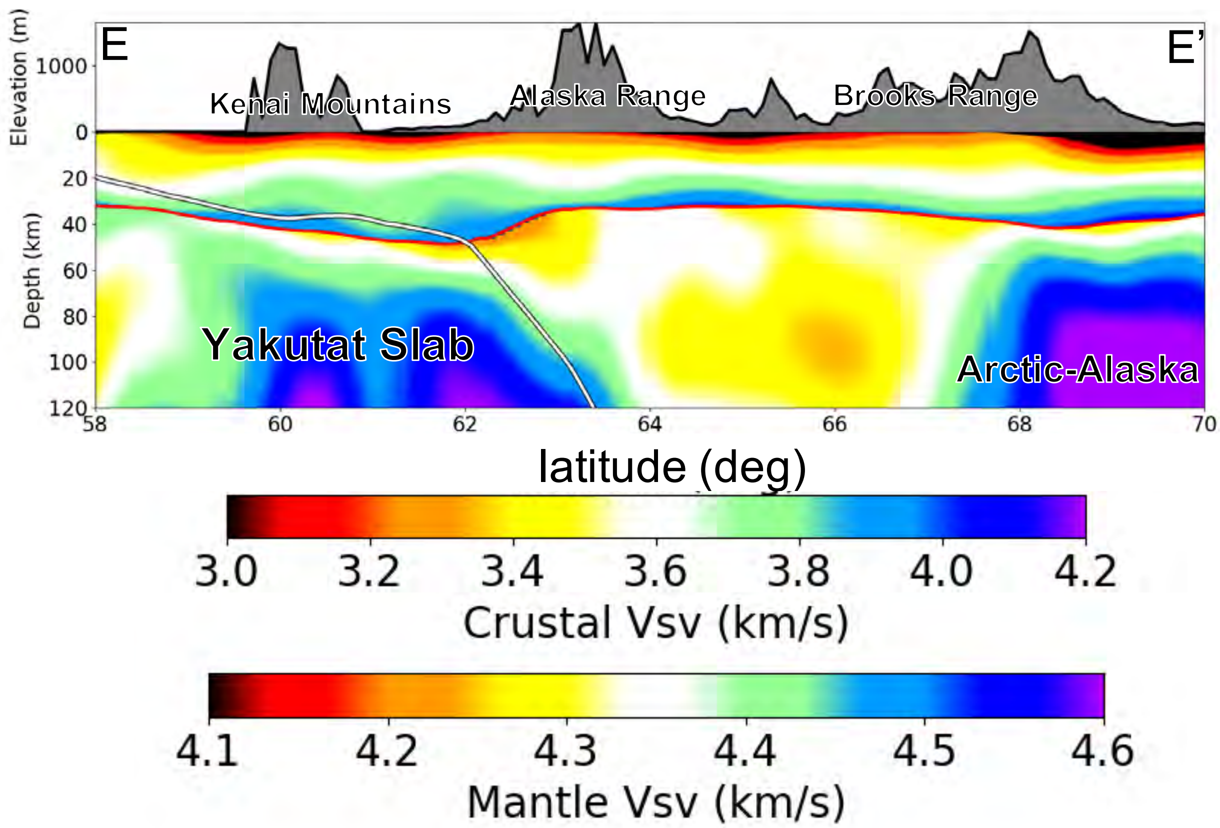

Figure 21. Vertical cross section E-E' identified in **Fig. 14b**. The white lines in the cross-sections identify the upper edge of the subducting lithosphere in the model of Jadamec and Billen (2010).

Table 1. Names of the structural features identified with abbreviations in Fig. 1.

Abbreviation	Name
AA	Arctic Alaska
BA	Back-Arc
BR	Brooks Range
CC	Canadian Cordillera
CMF	Castle Mountain Fault
CM	Chugach Mountains
DF	Denali Fault
INFF	Iditarod-Nixon Fork Fault
KF	Kaltag Fault
NAC	North American Craton
NS	North Slope
TF	Tintina Fault
WT	Wrangellia Terrane
WVF	Wrangell Volcanic Field
YCT	Yukon Composite Terrane
YT	Yakutat Terrane

Table 2. Description of seismic networks used in this study.

Network	Description
5C	Dynamics of Lake-Calving Glaciers: Yakutat Glacier, Alaska
7C	The Mackenzie Mountains Transect: Active Deformation from Margin to Craton
AK	Alaska Regional Network
AT	National Tsunami Warning System
AV	Alaska Volcano Observatory
CN	Canadian National Seismograph Network
II	Global Seismograph Network (GSN - IRIS/IDA)
IU	Global Seismograph Network (GSN - IRIS/USGS)
PN	PEPP-Indiana
PO	Portable Observatories for Lithospheric Analysis and Research Investigating Seismicity
PP	Princeton Earth Physics Program
TA	USArray Transportable Array (NSF EarthScope Project)
US	United States National Seismic Network
XE	Broadband Experiment Across Alaskan Range
XN	Canadian Northwest Experiment
XR	Structure and Rotation of the Inner Core (ARCTIC)
XY	Batholith Broadband
XZ	STEEP: St. Elias Erosion and Tectonics Project
YE	Bench Glacier Seismic Network
YM	Denali Fault Aftershocks RAMP
YV	Multidisiplinary Observations of Subduction (MOOS)
ZE	Southern Alaska Lithosphere and Mantle Observation Network

Table 3. Specification of the prior distribution of models. m_0 is the reference value for each variable.

Model parameters	Range
Sediment thickness	0-2 m_0 (km)
Crustal thickness	$m_0 \pm 0.5\ m_0$ (km)
Vs, top of sediment	0.2 – 2 (km/sec)
Vs, bottom of sediment	0.5 – 2.5 (km/sec)
B-spline coefficients, crust	$m_0 \pm 0.2\ m_0$ (km/sec)
Crustal anisotropy	± 10 %
B-spline coefficients, mantle	$m_0 \pm 0.2\ m_0$ (km/sec)
Mantle anisotropy	± 10 %

Table 4. Names of sedimentary basins identified with numbers in Fig. 11a.

Index	Name of the sedimentary basin
1	Bethel Basin
2	Bristol Bay Basin
3	Colville Basin
4	Cook Inlet Basin
5	Copper River Basin
6	Galena Basin
7	Hope Basin & Kotzbue Basin
8	Holtina Basin
9	Kobuk-Koyuku Basin
10	Nenana Basin
11	Norton Basin
12	Yakutat Basin
13	Yukon Flats Basin